

Mass-transferring binary stars as progenitors of interacting hydrogen-free supernovae

A. Ercolino¹, H. Jin¹, N. Langer^{1,2}, and L. Dessart³

¹ Argelander Institut für Astronomie, Auf dem Hügel 71, DE-53121 Bonn, Germany
e-mail: aercolino@astro.uni-bonn.de

² Max-Planck-Institut für Radioastronomie, Auf dem Hügel 69, DE-53121 Bonn, Germany

³ Institut d'Astrophysique de Paris, CNRS-Sorbonne Université, 98 bis boulevard Arago, F-75014 Paris, France

Received Month Day, 2024; accepted Month Day, 2024

ABSTRACT

Context. Stripped-envelope supernovae (SNe) are hydrogen-poor transients produced at the end of the life of massive stars that have previously lost most or all of their hydrogen-rich envelope. The progenitors of most stripped-envelope SNe are thought to be donor stars in mass transferring binary systems, which were stripped of their hydrogen-rich envelopes some 10^6 yr before core collapse. A subset of the stripped-envelope SNe exhibit spectral and photometric features indicative of early, intense interactions between their ejecta and nearby circumstellar material (CSM), occurring within days or weeks of the explosion.

Aims. We examine whether Roche lobe overflow during, or shortly before, core collapse in massive binary systems can produce the CSM inferred from the observations of interacting H-poor SNe.

Methods. We select 44 models from a comprehensive grid of detailed binary evolution models which are representative of the subset in which the mass donors are hydrogen-free and explode while transferring mass to a main-sequence companion. We characterize the properties of the pre-SN stellar models and of the material surrounding the binary at the time of the SN.

Results. We find that in these models, mass transfer starts less than ~ 20 kyr before, and often continues until the core collapse of the donor star. Up to $0.8 M_{\odot}$ of hydrogen-free material are removed from the donor star during this phase, of which a large fraction may be lost from the binary system and produce He-rich circum-binary material. We explore plausible assumptions for its spatial distribution at the time of explosion. When assuming that the CSM accumulates in a circumbinary disk, we find qualitative agreement with the supernova and CSM properties inferred from observed Type Ibn SNe, and to a lesser extent with constraints from Type Icn SNe. Considering the birth probabilities of our mass transferring stripped envelope SN progenitor models, we find that they may produce up to $\sim 10\%$ of all stripped envelope supernovae.

Conclusions. The generic binary channel proposed in this work can qualitatively account for the observed key properties and the observed rate of interacting H-poor SNe. Models for the evolution of the circumbinary material and for the spectral evolution of exploding progenitors from this channel are needed to further test its significance.

1. Introduction

Many massive stars end their lives as supernovae (SNe), bright transients which are observable even in distant galaxies. Past surveys (PTF, Law et al. 2009, and iPTF Kulkarni 2013), and especially ongoing ones (e.g., ATLAS, Tonry et al. 2018, ASAS-SN, Kochanek et al. 2017, ZTF, Bellm et al. 2019) have dramatically increased the number of observed SNe over the last few decades, which led to the discovery of new, particular SN types. This is expected to continue in the coming years and decades, particularly thanks to the beginning of new surveys such as LSST (Ivezic et al. 2019).

These surveys are providing growing evidence that the light of as much as $\sim 10\%$ of all core-collapse (CC)SNe is affected, sometimes even dominated, by the interaction of the SN ejecta with circumstellar material (CSM) surrounding the exploding star (e.g., Perley et al. 2020). The relatively slow-moving CSM can produce narrow-line features in the SN spectrum, which prompts the classification of such transients as Type IIn (with narrow H-emission lines), Type Ibn (He), Type Icn (C/O) and even Type Ien (S/Si, Schulze et al. 2024) SNe. In some instances, the interaction power is so strong as to result in super-luminous (SL)SNe (Chatzopoulos et al. 2012) and can also explain more exotic events like some Fast Blue Optical Transients (FBOTs, e.g., AT-2018cow, Margutti et al. 2019; Pellegrino et al.

2022b; Ho et al. 2023). The observed presence of CSM hence offers a valuable diagnostic for probing the late stages of stellar evolution.

Recent studies have investigated the characteristics of the CSM in interacting H-poor SNe, through explosion modeling (e.g., Dessart et al. 2022; Takei et al. 2024), or by analyzing the light-curves of observed events (e.g., Chatzopoulos et al. 2012, 2013). For Type Ibn and Icn SNe, not all events of the same class are associated with the same progenitor and CSM structure (e.g., Turatto & Pastorello 2014; Pellegrino et al. 2022a). Some, like the Type Ibn SN 2019uo, (Gangopadhyay et al. 2020), and the Type Icn SN 2022ann, (Davis et al. 2023) are highly energetic explosions associated to massive WR stars. Others, such as ultra-stripped (US) Type Ibn SN 2019dge (Yao et al. 2020), are much less energetic and likely originate from low-mass progenitors. These SNe prompt questions about the progenitors and the CSM required to explain the observations, as canonical single-star models struggle to reproduce the inferred CSM for these SNe.

Some works suggest that single stars can undergo strong phases of mass loss due to mechanisms such as thermonuclear flashes in the core (Woosley et al. 1980; Woosley & Heger 2015), wave-driven envelope excitations (Quataert & Shiode 2012; Wu & Fuller 2021), and LBV-type eruptions (Smith & Arnett 2014). If triggered shortly before CC, these mechanisms not only pro-

arXiv:2412.09893v1 [astro-ph.SR] 13 Dec 2024

duce the CSM, but also explain the observed pre-SN outbursts associated with some interacting SNe.

Most massive stars are born as members of close binary systems (Sana et al. 2012), of which many undergo mass transfer to their companion star through Roche lobe overflow (RLOF) during their evolution (Podsiadlowski et al. 1992). In most interacting binaries, this happens as a consequence of the post main-sequence expansion of the donor star, long before a supernova explosion occurs in the binary. However, some donor stars expand strongly after core helium exhaustion, which can trigger a late RLOF that continues until the mass donor's core collapses. For non-conservative mass transfer, this situation can lead to a dense CSM surrounding the binary system at the time of the supernova explosion. This is found in binary evolution models containing H-rich (Matsuoka & Sawada 2024; Ercolino et al. 2024) or H-poor donor stars (Wu & Fuller 2022a, referred to hereafter as WF22). This binary channel enables stars of the same initial mass to follow various evolutionary paths, depending on their initial orbital configuration, which may relate to the variety of Type II SNe progenitors (e.g., in wide binaries: Ouchi & Maeda 2017; Matsuoka & Sawada 2024; Ercolino et al. 2024; Dessart et al. 2024), as well as Type IIb (Claeys et al. 2011; Sravan et al. 2019; Yoon et al. 2017) and Type Ibc SNe (Yoon et al. 2010; Dessart et al. 2011).

In stripped-envelope SNe, the exploding star is a naked He star (HeS). It has been established that low-mass HeS ($\lesssim 3.5 M_{\odot}$) expand strongly after core-helium burning (e.g., Paczyński 1971; Habets 1986; Woosley et al. 1995; Wellstein & Langer 1999; Yoon et al. 2010; Kleiser et al. 2018; Woosley 2019; Laplace et al. 2020, WF22). In binaries, this expansion can trigger mass transfer. If some of the transferred mass escapes the system, it could form the CSM near the binary, which may interact with the ejecta during the first SN explosion that occurs in the binary.

In this paper, we investigate how interacting Type Ibc SNe can arise in binaries undergoing multiple phases of stable mass transfer. Unlike many studies that focus on binaries with compact object companions, such as a black hole (BH, e.g. Jiang et al. 2023) or a neutron star (NS, e.g. Tauris et al. 2013, 2015; Jiang et al. 2021, 2023; Guo et al. 2024, WF22), this work examines the more abundant systems where the exploding star is the initially more massive star in the binary, orbiting a main-sequence (MS) companion. Although such binaries have been modeled before, e.g. (Habets 1986; Laplace et al. 2020) and WF22, we use a comprehensive approach here with the aim of covering the diversity of pre-SN CSM structures and to explore the frequency with which they occur in the universe.

The paper is structured as follows. We begin by detailing the physics of the stellar evolutionary models (Sect. 2) and the parameter space for pre-SN mass transfer (Sect. 3). We then analyze binary evolution models and their pre-SN properties (Sect. 4) followed by the impact of the CSM on the SN (Sect., 5) before comparing between the model predictions with observed H-poor interacting SNe (Sect. 6). Finally, we discuss key physical processes and uncertainties that affect our results (Sect. 7) before summarizing the results (Sect. 8).

2. Method and assumptions

In this work, we study binary models that develop into HeS+MS systems undergoing mass transfer shortly before CC (which we refer to as Case BC RLOF, cf. Sect. 3.2). These systems are potential progenitors of interacting H-poor SNe, assuming that some of the transferred mass escapes to form the CSM.

Three series of stellar evolutionary models run with MESA (r10398, Paxton et al. 2011, 2013, 2015, 2018, 2019) are used. The first is a large-scale grid of previously calculated detailed binary evolutionary models (BG; Jin et al., in prep) which, due to the numerical settings used, do not produce many mass-transferring HeS+MS binaries (cf., Sect. 3). To expand the coverage of systems undergoing Case BC RLOF, we produce two other sets of models. The first is a set of detailed single HeS models, used to diagnose models in the BG set where the stripped primary (i.e., the initially more massive star) is expected to expand and trigger Case BC RLOF. By comparing the BG set with the single HeS models, we select and run a representative set of the BG models up to CC, using improved physics and numerical settings to better tackle their evolution. Throughout this work, we refer to the HeS primary in a binary system as a binary-stripped HeS, in contrast to a single HeS model.

The three sets of models share key settings as described in Ercolino et al. (2024) and Jin et al. (2024), including the initial metallicity ($Z = Z_{\odot}$, with $Z_{\odot} = 0.0154$ from Asplund et al. 2021), and wind mass-loss prescription. In the following, we present the differences in the physics assumptions between the sets.

2.1. Initialization and rotation

In both the BG set and our binary models, each star is initialized at ZAMS with an initial rotation set to 20% of its breakup velocity (Dufton et al. 2013).

The single HeS models are initialized following Aguilera-Dena et al. (2022, 2023), where a MS star is evolved with artificial full mixing and no winds until core H depletion. Afterwards, artificial mixing is disabled and the winds are introduced, allowing the model to evolve as a HeS. Rotation is neglected in single HeS models as in the BG set, the binary-stripped HeS models rotate very slowly during core He burning.

2.2. Nuclear network and termination

The BG set adopts the stern nuclear network (Heger et al. 2000; Jin et al. 2024), and the models are terminated after the end of core C-burning, (Jin et al., in prep; however some models are also terminated beforehand, see Sect. 2.4).

We adopt the approx21 network in the single and binary-stripped HeS models, as it includes the bare minimum number of isotopes to evolve the models until CC. As our parameter space focuses on low-mass cores (cf. Sect. 3), the nuclear network adopted here is suboptimal (cf., Farmer et al. 2016). The next smallest viable nuclear network in MESA, which contains 75 isotopes, increases the computation time, hindering the feasibility of running a grid of models.

2.3. Overshooting and non-adiabatic convection

Overshooting is included in the convective H-burning core based on the initial mass, following Hastings et al. (2021). After core H-burning, overshooting is not included in any of the convective boundaries until the end of core C burning. After core C burning, when the models in the BG set are terminated, our single and binary-stripped HeS models introduce small-scale over and undershooting across all convective boundaries, extending only $0.008H_P$ from the boundary (with H_P being the local pressure scale height at the convective boundary). This reduces computation difficulties, especially as successive core burning phases ignite off-center, causing convergence issues. Given the number

of convective regions that develop as heavier elements are burnt, the adoption of convective over and undershooting may yield considerable differences in the final core structure.

Lastly, the BG set adopts MLT++ (Paxton et al. 2015) to handle convectively unstable regions with inefficient energy transport (i.e., subsurface convective regions) by artificially reducing the local superadiabaticity. This can lead to smaller radii in models with convective layers near the surface, as well as density inversions. We therefore employ the standard MLT in both our single- and binary-stripped HeS models, rather than MLT++.

2.4. Roche lobe overflow

The BG grid of models adopts different mass transfer schemes depending on the primary star’s evolutionary phase. If the primary is still a MS star, the mass transfer scheme is the ‘contact’ scheme (Marchant et al. 2016). After the MS, the mass transfer scheme adopted is that of Kolb & Ritter (1990) to handle RLOF from a convective envelope.

Since we run binary models that begin RLOF after the MS (cf. Sect. 3), we adopt the scheme from Kolb & Ritter (1990), where we also consider the radiation pressure of the donor star in the mass-transfer calculation, as done in WF22. Our treatment is the same as that in Ercolino et al. (2024). We assume that the transferred mass also carries angular momentum and that accretion is halted when the accretor reaches critical rotation (Petrovic et al. 2005). In the models from the BG set, this typically results in a small amount of mass being accreted, around $\lesssim 0.3 M_{\odot}$ during Case B RLOF. The mass that fails to be accreted is assumed to be lost from the binary system, carrying away the specific angular momentum of the accreting star. We assume that Case BC RLOF is completely inefficient (see Sect. 4.1).

In the BG set, a model is terminated when unstable mass transfer and therefore common envelope (CE) evolution ensue. Unstable RLOF is assumed to occur if the model exhibits inverse mass transfer, RLOF at ZAMS, Darwin instability (Darwin 1879), or if it becomes an overcontact binary outflowing material from the L2 point. An additional stopping condition in the BG set occurs when a model reaches a mass transfer rate of $10^{-1} M_{\odot} \text{ yr}^{-1}$. We do not apply this condition in our binary models. We additionally consider mass transfer to turn unstable when the donor star reaches the volume-equivalent radius associated to its outer Lagrangian point ($\sim 1.3R_{\text{RL},1}$, Marchant et al. 2021). This can lead to outer Lagrangian-point outflows (OLOF, Pavlovskii & Ivanova 2015; Ercolino et al. 2024). These conditions provide a broad parameter space to investigate models (but see Sect. 7.2.2 for a discussion using different assumptions).

3. Parameter Space

The key ingredient for an interacting H-poor SN is the presence of a dense, H-poor CSM. Assuming that the CSM forms from the material not accreted by the companion star during RLOF shortly before CC, we search for H-poor donors that will undergo Case BC RLOF.

Since the BG set underestimates the parameter space for models undergoing Case BC RLOF (cf. Sect. 3.2), we aim to identify the systems that are expected to do so. We first investigate the radial expansion of single HeS models in their later evolutionary stages (Sect. 3.1). We then compare the single HeS models with the binary-stripped HeS models in the BG set at the end of core He burning to assess which models are expected to undergo RLOF before CC (Sect. 3.2). This enables us to select the initial parameters of the models to recompute (Sect. 3.3).

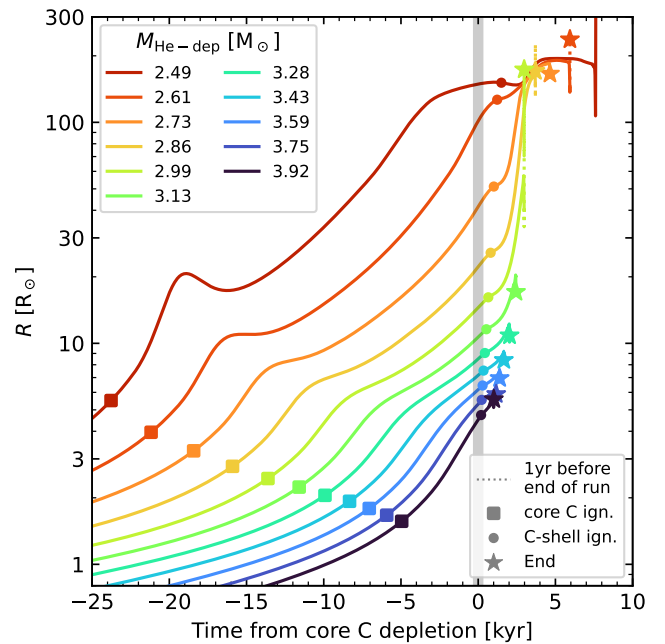


Fig. 1. Evolution of the radius of single HeS models as a function of time during and after core carbon burning, with $t = 0$ set at core carbon depletion. The square markers indicate core carbon ignition, circles indicate the time when the first carbon shell develops, and stars mark the end of the calculation. For the lowest mass model, no endpoint is shown (see Sect. 3.1).

3.1. Single HeS models

We compute single HeS models with initial masses between 2.99 and $5.31 M_{\odot}$ and focus on their radius evolution (cf. Table 1 and Fig. 1).

During core He burning, these stars have radii below $\sim 1 R_{\odot}$. Stellar winds reduce their mass over time, resulting in a decrease of the convective He-burning core mass, which affects the final CO-core mass. We label the models by their mass at core He-depletion ($M_{\text{He-dep}}$), prefixed with ‘He’. For example, model He2.49 is the lowest-mass model, with an initial mass $M_i = 2.99 M_{\odot}$ and $M_{\text{He-dep}} = 2.49 M_{\odot}$.

After core He-burning, shell He-burning drives the expansion of the He-rich envelope, which is more significant for lower mass models (cf., Fig. 1). The expansion continues during C-burning. In the lowest mass models, the expansion temporarily stalls (models He2.49, and He2.61), due to the more significant decrease of the power of the He-burning shell. The stellar expansion continues beyond core-C exhaustion. In the $\sim 2 - 3$ kyr that follow the ignition of the first C-burning shell, the radius grows significantly, with the lowest mass models reaching $\sim 200 R_{\odot}$. More massive models (with $M_{\text{He-dep}} > 3.59 M_{\odot}$) explode before they can expand significantly. Following C-shell burning, the He-burning shell becomes convective for all models. In the least massive models, which developed the largest radii (i.e., models from He2.49 to He2.99), the outer envelope also turns convective.

After Ne and O ignite in the core, the envelope contracts significantly in smaller-mass models (cf. Fig. 1) but remains largely unaffected in higher-mass ones. Models He2.86 and He2.99 exhibit ingestion of He inside the CO-core shortly before core-Si ignition, causing the envelope to expand or oscillate significantly. In models He2.61 and He2.49, the surface and the He-

Table 1. Properties of the single HeS models.

M_i	$M_{\text{He,conv}}^{\text{max}}$	$M_{\text{He-dep}}$	$M_{\text{CO,max}}$	$\Delta t_{\text{C-end}}$	$R_{\text{max}}^{20\text{kyr}}$	$R_{\text{max}}^{10\text{kyr}}$	$R_{\text{max}}^{5\text{kyr}}$	$R_{\text{max}}^{1\text{kyr}}$	$R_{\text{max}}^{1\text{yr}}$	R_{max}	$\log \rho_c$	$\log T_c$	$\log T_{\text{max}}$	End
M_{\odot}	M_{\odot}	M_{\odot}	M_{\odot}	kyr	R_{\odot}	R_{\odot}	R_{\odot}	R_{\odot}	R_{\odot}	R_{\odot}	g cm^{-3}	K	K	of run
(1)	(2)	(3)	(4)	(5)	(6)	(7)	(8)	(9)	(10)	(11)	(12)	(13)	(14)	(15)
2.99	1.16	2.49	1.38	31.8	23.4	133	152	195	499	4254	8.93	8.77	9.11	Ne ^{EC*}
3.16	1.26	2.61	1.43	27.0	11.0	36.0	123	191	191	237	9.07	9.00	9.49	Ne/O*
3.35	1.36	2.73	1.52	23.1	5.37	15.3	37.7	171	185	185	8.03	9.03	9.44	O
3.55	1.48	2.86	1.61	19.6	2.64	8.90	17.4	74.6	166	225	8.89	9.34	9.56	Si*
3.76	1.61	2.99	1.70	16.6	1.79	6.39	10.6	21.0	57.4	173	8.81	9.22	9.58	Si*
3.98	1.75	3.13	1.80	14.0	1.41	4.28	7.55	12.9	20.4	20.4	7.94	9.23	9.57	Si
4.22	1.90	3.28	1.91	12.0	1.17	2.63	5.97	9.54	12.2	12.2	9.53	9.84	9.84	Si
4.47	2.06	3.43	2.02	10.0	0.99	1.91	4.61	7.69	9.14	9.14	10.2	10.0	10.0	CC
4.73	2.24	3.59	2.14	8.4	0.84	1.51	3.19	6.50	7.50	7.50	10.2	10.0	10.0	CC
5.01	2.43	3.75	2.28	7.1	0.72	1.24	2.27	5.48	6.36	6.36	10.1	10.0	10.0	CC
5.31	2.64	3.92	2.41	6.0	0.62	1.05	1.78	4.52	5.51	5.67	10.1	9.99	9.99	CC

Notes. The columns show the initial mass (1), the maximum extent of the convective He-burning core (2), the mass at core helium depletion (3), the maximum mass of the CO-core (4), the time between core C-ignition and the end of the run (5), the maximum radius exhibited between core He-depletion and 20 kyr before the end of the run (6), 10 kyr (7), 5 kyr (8), 1 kyr (9), 1 yr (10), and the absolute maximum value (11). Columns 12-14 show the central density, central and maximum temperature in the model at the 6end of the run respectively. Column 15 highlights the burning phase at the end of the run labeled according to the nuclei being burnt, if it didn't reach CC because of numerics. (*) Models have experienced a strong expansion of the envelope before terminating (see Sect. 3.1). (EC) The lowest-mass model is expected to end as an EC-SN.

burning convective regions merge, leading to significant radius expansion.

The key results of the simulations are shown in Table 1. All models, except the least massive, are expected to end their evolution as CC-SNe, even though many terminated shortly before CC. In particular, the models' central density and temperature increase towards the end of the run, resembling the CC progenitors in Tauris et al. (2015). The lowest-mass model in the set (He2.49) evolves with an almost constant central temperature (below that achieved during core C burning) and increasing densities, resembling the electron-capture (EC) SN progenitor in Tauris et al. (2015). HeS models with masses similar to that of model He2.49 are expected to explode as EC-SNe, while those at lower masses will turn into a WD.

These models enable mapping the radius evolution as a function of mass of the HeS. We build a mass-radius diagram (cf. Fig. 2) showing how long before CC a single HeS of mass $M_{\text{He-dep}}$ reaches a radius R .

3.2. Comparing HeS models to the BG set

Using the mass-radius map from single HeS models (Sect. 3.1), we identify the binary-stripped HeS models likely to undergo Case BC RLOF. This is done by comparing their Roche lobe radius ($R_{\text{RL},1}$) with the expected radius evolution of a single HeS model with the same $M_{\text{He-dep}}$. We focus exclusively on models undergoing Case B RLOF as the first phase of mass-transfer. We briefly discuss Case A systems in Appendix A.

For systems where Case B is the first mass-transfer phase, the donor does not lose a fixed amount of mass or the entire H-rich envelope, as often assumed in rapid-binary evolution codes (e.g., ComBinE; Kruckow et al. 2018). Rather, the amount of mass-loss depends on the initial mass ratio (q_i) and orbital period (P_i), leading to varying degrees of stripping for primaries of same initial mass ($M_{1,i}$). Moreover, during core He burning, core growth depends on the mass of the leftover H-rich envelope (e.g., Ercolino et al. 2024). If the H-envelope mass is $\lesssim 1 M_{\odot}$, the long timescales for core-He burning allow stellar winds to shed it away entirely (though wind mass-loss rates are uncertain, see

Sect. 7.1). These effects lead to the differences of up to $1 M_{\odot}$ in $M_{\text{He-dep}}$ in stars of the same $M_{1,i}$ found in binaries (see Fig. 3).

All Case B models in the BG set exhibit $R_{\text{RL},1} \gtrsim 5 R_{\odot}$ during core He burning, which is larger than the maximum radius expected from single HeS models in that phase (cf. Sect. 3.1). This implies that RLOF can only occur after core He depletion. Following core He depletion, the timescales ensure that wind mass loss from either star does not significantly alter the orbital configuration, leaving $R_{\text{RL},1}$ unchanged until the onset of another phase of RLOF or CC.

To identify models that will undergo Case BC RLOF, we compare $R_{\text{RL},1}$ at core He-depletion with the maximum radius of a single HeS model of the same mass $M_{\text{He-dep}}$. Figure 3 shows that there is a much larger parameter space for systems undergoing Case BC RLOF, compared to the BG set. This difference likely stems from the adoption of MLT++ in the BG set and the termination of the calculation at core C depletion (cf. Fig. 1). Models expected to undergo Case BC RLOF are concentrated at low initial $M_{1,i}$, low q_i and low P_i .

We find boundaries in the initial mass for the parameter space where the primary undergoes CC following Case BC RLOF. Binary-stripped HeS models produce CCSNe only for $M_{1,i} \geq 11.2 M_{\odot}$. On the other hand, models with $M_{1,i} > 15.8 M_{\odot}$ develop $M_{\text{He-dep}} > 3.6 M_{\odot}$ and do not expand enough to fill their Roche lobes again.

3.3. Initial conditions for the representative set of models to rerun

We rerun a representative set of the models in the BG grid, based on the comparison with our single HeS models in Sect. 3.2. Assuming that the CSM forms from the unaccreted mass during Case BC RLOF, this defines a clear parameter space to study interacting H-poor SN progenitors (Fig. 2).

Models occupying similar points in mass-radius diagram (Fig. 2) can originate from different q_i , P_i and $M_{1,i}$, resulting in significantly different companion masses (M_2). We argue that the effect of different M_2 have a secondary impact on the amount of mass removed during Case BC RLOF (see Appendix B).

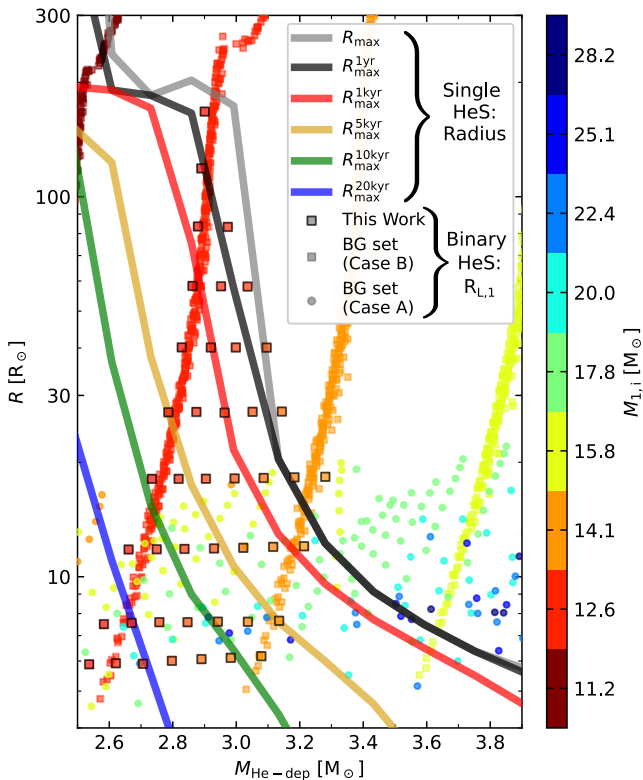


Fig. 2. Mass-radius diagram for single HeS models (showing the stellar radius, lines) and binary-stripped HeS models (showing the Roche lobe radius, symbols) as a function of the mass at core He-depletion $M_{\text{He-dep}}$. For single HeS models, the radius at a time t before the end of the run (R_{max}^t) is plotted for different t (see legend). Binary-stripped HeS models are shown for different initial primary masses $M_{1,i}$ (see colorbar), and different markers are used for Case A (circles) and Case B systems (squares). The binary-stripped HeS models are distinguished between those from the BG set (without outline), and this work (black outline).

Under these assumptions, the parameter space for interacting H-poor SNe is defined by two variables: $M_{\text{He-dep}}$ and $R_{\text{RL},1}$. We will work with Case B systems, which are favored by the IMF (see Appendix A). Case B systems also offer a convenient degeneracy in the grid (see Figs. 2 and 3). For a given initial mass $M_{1,i}$, there is a one-to-one correlation between $R_{\text{RL},1}$ and $M_{\text{He-dep}}$ enabling the tracing of distinct progenitor systems with different (q_i, P_i) .

We rerun a subset of these models at $q_i = 0.50$. This choice reflects that systems with lower q_i are more likely to experience unstable mass transfer during Case B RLOF, while those at higher q_i have a narrower range of P_i for which systems undergo Case BC RLOF (cf., Fig. 3). We chose initial masses of $12.3 M_{\odot} \leq M_{1,i} \leq 14.1 M_{\odot}$ (in logarithmic steps of 0.01, instead of 0.05 from the BG set). The initial orbital period P_i is selected adaptively to only include binaries that are expected to undergo Case BC RLOF with $P_i > 5$ d (cf. Table 2).

4. Results

In this section, we present the results of the rerun binary models. In Sect. 4.1 we will focus on one specific model, followed by Sect. 4.2 with an overview across all the models. We discuss the generic features of the SN progenitors in Sect. 4.3 with a brief discussion on the post-SN evolution of these systems in Sect. 4.4.

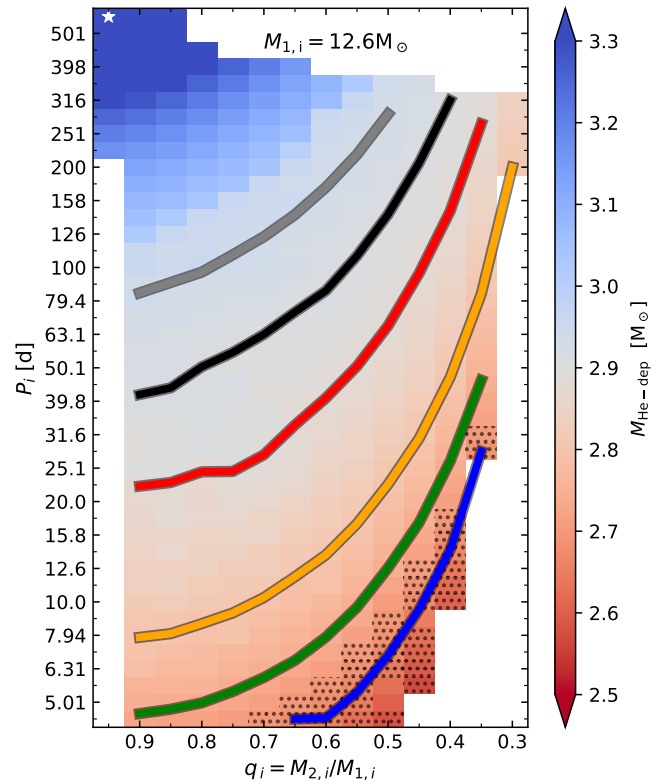


Fig. 3. The $\log P_i - q_i$ diagram for the BG grid with $M_{1,i} = 12.6 M_{\odot}$, where each pixel represents one detailed binary evolution model. The color coding represents the mass of the primary star at core helium depletion. The solid lines cover the models where the radius of a single HeS of the same mass (cf. Fig. 2) matches their Roche lobe radius at core He depletion. White pixels are models that terminated before core-carbon ignition (see Sect. 2.4). The dotted patches correspond to the models which exhibited Case BC RLOF in the BG set. The star marker in the top-left corner corresponds to the lowest-period model shown in Ercolino et al. (2024).

4.1. Example Model

Here, we examine the evolution of a single model, with $M_{1,i} = 13.5 M_{\odot}$, $q_i = 0.50$ and $P_i = 6.3$ d (Fig. 4).

4.1.1. Case B mass transfer and subsequent stripping

Both stars evolve effectively as single stars until after the primary reaches TAMS. The primary then expands, filling its Roche lobe and initiating mass transfer. During this phase, most of the H-rich envelope is quickly stripped until nuclear-processed material from the core is exposed. This material, initially part of the convective H-burning core, remains H-rich but is He- and N-enhanced (cf. Fig. 4). At this point, $8.3 M_{\odot}$ of the envelope have been removed, and mass transfer becomes less intense, removing an additional $0.77 M_{\odot}$. Mass transfer stops as the primary star ignites He, leaving behind a $0.67 M_{\odot}$ envelope and a $3.31 M_{\odot}$ He-core.

During core He-burning, the He-core initially grows to $3.57 M_{\odot}$ due to the H-burning shell. Stellar winds also contribute to the erosion of the envelope, which is lost 340 kyr after Case B RLOF. At this point, the primary star is a HeS. Over the remaining phase of core He burning ($\sim 10^6$ yr), the primary star sheds $0.59 M_{\odot}$ of its He-rich envelope via winds, reaching core He-depletion with $M_{\text{He-dep}} = 2.94 M_{\odot}$.

Table 2. Key parameters for the binary-models rerun in this work.

$M_{1,i}$		Case B RLOF		Core He burning					Core He-dep		Case BC RLOF				End						
$M_{1,i}$	P_i	ΔM_1	ΔM_2	Δt	$M_{\text{conv}}^{\text{max}}$	L	\mathcal{L}	T_{eff}	M_1	$R_{\text{RL},1}$	Δt	ΔM_1	$\dot{M}_{\text{max}}^{(-)}$	Δt_{max}	M_1^{\dagger}	M_{CO}^{\dagger}	$\langle Z \rangle_{\text{env}}^{\dagger}$	$\log \rho_c$	$\log T_c$	$\log T_{\text{max}}$	End
(1)	(2)	(3)	(4)	(5)	(6)	(7)	(8)	(9)	(10)	(11)	(12)	(13)	(14)	(15)	(16)	(17)	(18)	(19)	(20)	(21)	(22)
M_{\odot}	d	M_{\odot}	M_{\odot}	Myr	M_{\odot}	kL_{\odot}	kL_{\odot}	kK	M_{\odot}	R_{\odot}	kyr	M_{\odot}	$10^{-4} M_{\odot} \text{ yr}^{-1}$	kyr	M_{\odot}	M_{\odot}		g cm^{-3}	K	K	of run
12.3	5.01	8.61	0.26	1.72	1.3	8.66	3.02	80.0	2.53	5.88	26.1	0.79	1.18	4.19	1.62	1.44	0.14	7.68	8.68	9.27	Ne ^{EC}
12.3	6.31	8.57	0.21	1.67	1.32	9.30	3.16	80.1	2.58	7.51	23.2	0.78	1.35	3.61	1.68	1.46	0.19	8.71	9.00	9.42	Ne/O/Si*
12.3	10.0	8.50	0.18	1.60	1.36	10.5	3.43	79.9	2.66	11.8	13.7	0.74	1.95	2.64	1.81	1.50	0.19	8.26	9.07	9.51	Ne/O/Si
12.3	15.8	8.45	0.15	1.53	1.38	11.5	3.64	79.3	2.73	18.1	8.44	0.70	2.85	1.95	1.92	1.53	0.16	8.26	9.11	9.43	Ne/O
12.3	25.1	8.42	0.15	1.49	1.40	12.2	3.79	78.7	2.78	27.1	4.98	0.57	3.10	1.15	2.10	1.55	0.12	8.21	9.12	9.39	O
12.3	39.8	8.39	0.16	1.45	1.41	12.8	3.91	78.1	2.83	40.1	2.22	0.41	2.92	0.67	2.30	1.57	0.10	8.83	9.21	9.58	Si*
12.3	63.1	8.36	0.16	1.43	1.42	13.2	4.01	77.6	2.86	58.2	1.52	0.28	2.85	0.02	2.46	1.58	0.09	8.79	9.34	9.55	Si
12.3	100	8.35	0.16	1.43	1.44	13.6	4.08	77.2	2.88	83.5	1.13	0.18	2.96	0.02	2.58	1.59	0.08	8.84	9.34	9.55	Si
12.3	158	8.33	0.17	1.43	1.46	13.8	4.13	77.1	2.89	119	0.78	0.10	1.75	0.15	2.67	1.61	0.07	8.68	9.35	9.55	Si
12.3	251	8.32	0.16	1.43	1.47	14.0	4.18	76.8	2.90	168	/	/	/	/	2.78	1.62	0.06	7.80	9.07	9.50	Ne/O/Si
12.6	5.01	8.75	0.26	1.64	1.37	9.59	3.22	81.2	2.62	5.92	22.5	0.78	1.28	3.27	1.72	1.48	0.20	8.55	9.03	9.44	Ne/O/Si*
12.6	6.31	8.71	0.20	1.59	1.40	10.3	3.38	81.4	2.67	7.56	19.5	0.76	1.49	2.73	1.79	1.51	0.20	7.93	9.01	10.2	Ne/O/Si
12.6	10.0	8.64	0.19	1.52	1.44	11.6	3.65	81.2	2.75	11.8	10.4	0.71	2.30	1.84	1.93	1.56	0.18	8.85	9.21	9.57	Si*
12.6	15.9	8.59	0.15	1.47	1.46	12.6	3.86	80.6	2.82	18.1	5.70	0.54	2.79	0.94	2.16	1.59	0.13	8.85	9.33	9.56	Si*
12.6	25.1	8.55	0.13	1.42	1.48	13.4	4.02	80.0	2.87	27.1	2.24	0.31	2.57	0.37	2.45	1.61	0.09	8.70	9.23	9.57	Si*
12.6	39.8	8.52	0.16	1.39	1.49	14.0	4.15	79.4	2.92	40.1	1.16	0.16	2.26	0.04	2.64	1.63	0.08	8.63	9.34	9.56	Si*
12.6	63.1	8.49	0.17	1.37	1.50	14.5	4.25	79.0	2.95	58.1	0.65	0.06	1.65	0.04	2.77	1.64	0.07	8.78	9.37	9.55	Si*
12.6	100	8.48	0.17	1.36	1.51	14.9	4.32	78.6	2.97	83.3	0.28	0.01	1.34	0.02	2.84	1.65	0.07	8.70	9.24	9.57	Si*
12.9	5.01	8.89	0.32	1.56	1.45	10.6	3.43	82.5	2.70	5.90	19.26	0.77	1.38	2.50	1.81	1.53	0.21	9.09	9.31	9.51	Si*
12.9	6.31	8.84	0.21	1.52	1.49	11.4	3.60	82.6	2.76	7.59	15.35	0.74	1.70	1.99	1.90	1.56	0.20	8.57	9.26	9.38	Si
12.9	10.0	8.77	0.20	1.46	1.52	12.7	3.87	82.5	2.83	11.8	7.66	0.61	2.49	1.06	2.11	1.62	0.14	8.76	9.21	9.57	Si*
12.9	15.9	8.72	0.16	1.41	1.55	13.8	4.09	82.1	2.90	18.1	3.47	0.29	2.53	0.02	2.50	1.65	0.10	8.85	9.45	9.98	Si*
12.9	25.1	8.68	0.16	1.37	1.56	14.7	4.26	81.5	2.96	27.0	1.04	0.10	1.87	0.03	2.75	1.68	0.08	9.02	9.40	10.0	Si*
12.9	39.8	8.65	0.16	1.34	1.58	15.3	4.38	81.0	3.00	40.1	0.40	0.02	1.04	0.03	2.86	1.69	0.08	8.56	9.43	9.57	Si*
12.9	63.1	8.62	0.17	1.32	1.59	15.9	4.49	80.5	3.03	58.0	/	/	/	/	2.92	1.71	0.07	8.46	9.44	9.56	Si
13.2	5.01	9.02	0.29	1.49	1.53	11.7	3.67	83.7	2.79	6.01	16.1	0.76	1.54	1.77	1.92	1.59	0.21	8.90	9.33	9.54	Si*
13.2	6.31	8.98	0.26	1.45	1.56	12.5	3.83	83.8	2.84	7.59	11.4	0.71	1.96	1.29	2.02	1.62	0.18	8.84	9.35	9.55	Si*
13.2	10.0	8.90	0.20	1.39	1.61	14.0	4.11	83.8	2.93	11.9	5.30	0.41	2.40	0.33	2.41	1.68	0.10	8.41	9.42	9.57	Si
13.2	15.9	8.84	0.16	1.35	1.64	15.1	4.33	83.4	2.99	18.1	1.35	0.10	1.79	0.02	2.77	1.72	0.08	8.30	9.53	9.57	Si
13.2	25.1	8.80	0.14	1.32	1.66	16.1	4.52	82.9	3.05	27.2	0.26	0.01	0.57	0.03	2.93	1.75	0.08	8.71	9.52	9.55	Si*
13.2	39.8	8.77	0.16	1.29	1.67	16.8	4.65	82.4	3.09	40.1	/	/	/	/	2.98	1.76	0.08	8.27	9.53	9.56	Si
13.5	5.01	9.15	0.29	1.42	1.63	13.0	3.91	84.9	2.89	6.07	13.0	0.72	1.75	1.12	2.05	1.66	0.17	8.77	9.38	9.55	Si*
13.5	6.31	9.11	0.27	1.38	1.66	13.8	4.08	85.1	2.94	7.62	8.57	0.60	2.15	0.60	2.23	1.69	0.13	9.00	9.37	9.43	Si*
13.5	10.0	9.03	0.21	1.33	1.71	15.3	4.36	85.1	3.02	11.9	3.41	0.18	2.08	0.02	2.72	1.74	0.09	8.73	9.24	9.57	Si*
13.5	15.9	8.97	0.16	1.29	1.73	16.5	4.58	84.8	3.08	18.2	0.50	0.02	0.76	0.01	2.95	1.78	0.09	8.74	9.50	9.55	Si*
13.5	25.1	8.92	0.14	1.26	1.75	17.6	4.77	84.3	3.14	27.2	/	/	/	/	3.03	1.81	0.08	7.86	9.54	9.57	Si
13.8	5.01	9.28	0.31	1.36	1.72	14.3	4.15	86.1	2.98	6.12	10.2	0.63	1.94	0.55	2.24	1.72	0.15	8.44	9.35	9.56	Si*
13.8	6.31	9.24	0.28	1.32	1.75	15.2	4.33	86.3	3.03	7.61	6.38	0.40	2.36	0.02	2.52	1.76	0.12	8.22	9.53	9.56	Si
13.8	10.0	9.16	0.21	1.28	1.80	16.7	4.61	86.4	3.11	12.0	1.66	0.05	1.14	0.01	2.95	1.81	0.09	7.86	9.51	9.54	Si
13.8	15.9	9.10	0.17	1.24	1.84	18.1	4.84	86.1	3.18	18.3	/	/	/	/	3.07	1.84	0.09	10.1	10.0	10.0	CC
14.1	5.01	9.41	0.32	1.30	1.83	15.7	4.41	87.3	3.08	6.18	7.56	0.44	2.14	0.02	2.53	1.79	0.12	7.88	9.54	9.57	Si
14.1	6.31	9.37	0.31	1.26	1.86	16.7	4.59	87.6	3.13	7.66	4.51	0.21	1.76	0.01	2.81	1.82	0.10	7.83	9.52	9.55	Si
14.1	10.0	9.28	0.23	1.22	1.91	18.3	4.87	87.7	3.21	12.0	0.43	0.01	0.41	0.01	3.09	1.88	0.09	10.2	10.0	10.0	CC
14.1	15.9	9.22	0.17	1.19	1.94	19.7	5.11	87.4	3.28	18.3	/	/	/	/	3.17	1.92	0.09	10.2	10.0	10.0	CC

Notes. The rows are grouped by models with the same initial primary mass M_1 . The columns are divided in different groups, for different evolutionary phases. Columns 1 and 2 show the initial conditions: the initial primary mass (Col. 1) and initial orbital period (2). Columns 3 and 4 show the amount of mass shed by the primary (3) and accreted by the secondary (4) during Case B RLOF. Columns 5-9 show parameters during core He burning: the time spent in this phase (5), the maximum extent in mass of the convective core (6), the average luminosity, spectroscopic luminosity and effective temperature of the primary (7-9, with a standard deviation of about $\sim 10\%$). Columns 10-11 show the parameters at core He depletion: the mass of the primary (10) and the Roche lobe radius (11). Columns 12-15 show parameters associated to Case BC RLOF: the time between the end of the run and the onset of Case BC RLOF (12), the amount of mass shed by the primary (13), the maximum mass transfer rate in units of $10^{-4} M_{\odot} \text{ yr}^{-1}$ (14) and the time before the end of the run at which the maximum mass transfer rate was reached (15). Columns 16-22 show the parameters at the end of the run: the final mass of the primary (16), its CO-core mass (17), the average metal abundance in the envelope (18), central density and temperature (19-20), the maximum temperature (21) and the burning phase at the end of the run labeled according to the nuclei being burnt, if it didn't reach CC (22). (*) Models have experienced Case X RLOF (see Sect. 4.2.3). (EC) The least-massive model is expected to end as an EC-SN. (†) The data is taken at 1 year before the end of the run to filter out the effects of Case X RLOF.

The secondary star spins up to critical rotation during RLOF due to the accretion of angular momentum. The time before the CC of the donor star is insufficient for a significant slow down. The secondary is therefore expected to appear as a Be star, both before and after the CC of the primary.

4.1.2. Case BC mass transfer

Comparison the single HeS models of similar mass shows that the primary star will expand to fill its Roche lobe ($7.6 R_{\odot}$) roughly 10 kyr before collapse (cf. Fig. 1 and Fig. 2).

Figure 4 shows that 8.7 kyr before CC, the primary began Case BC RLOF, reaching a maximum rate of $\sim 2 \times 10^{-4} M_{\odot} \text{ yr}^{-1}$ as the first C-burning shell turns off. By the end of core-O burn-

ing, RLOF removed about $0.71 M_{\odot}$ from the He-rich envelope, which now has a mass of $0.52 M_{\odot}$ with an average metal abundance $\langle Z \rangle = 0.13$ (mostly C, N and O).

4.1.3. Case X mass transfer

Following radiatively Si-burning, a thin Ne-burning shell ignites at the outer edge of the CO-core. The resulting convective region merges with the He-rich convective shell above (cf. Fig. 5), leading to ingestion of He in hotter and denser layers. He is now burnt at higher densities and temperatures, increasing the shell's luminosity, while metal-rich material is dredged-up, raising the envelope's opacity. The envelope becomes fully convective, and the radius expands significantly from 10 to $56 R_{\odot}$ in ~ 20 d (cf.

$$M_{1,i} = 13.5 M_{\odot}, \quad q_i = 0.5, \quad P_i = 6.3 \text{ d}$$

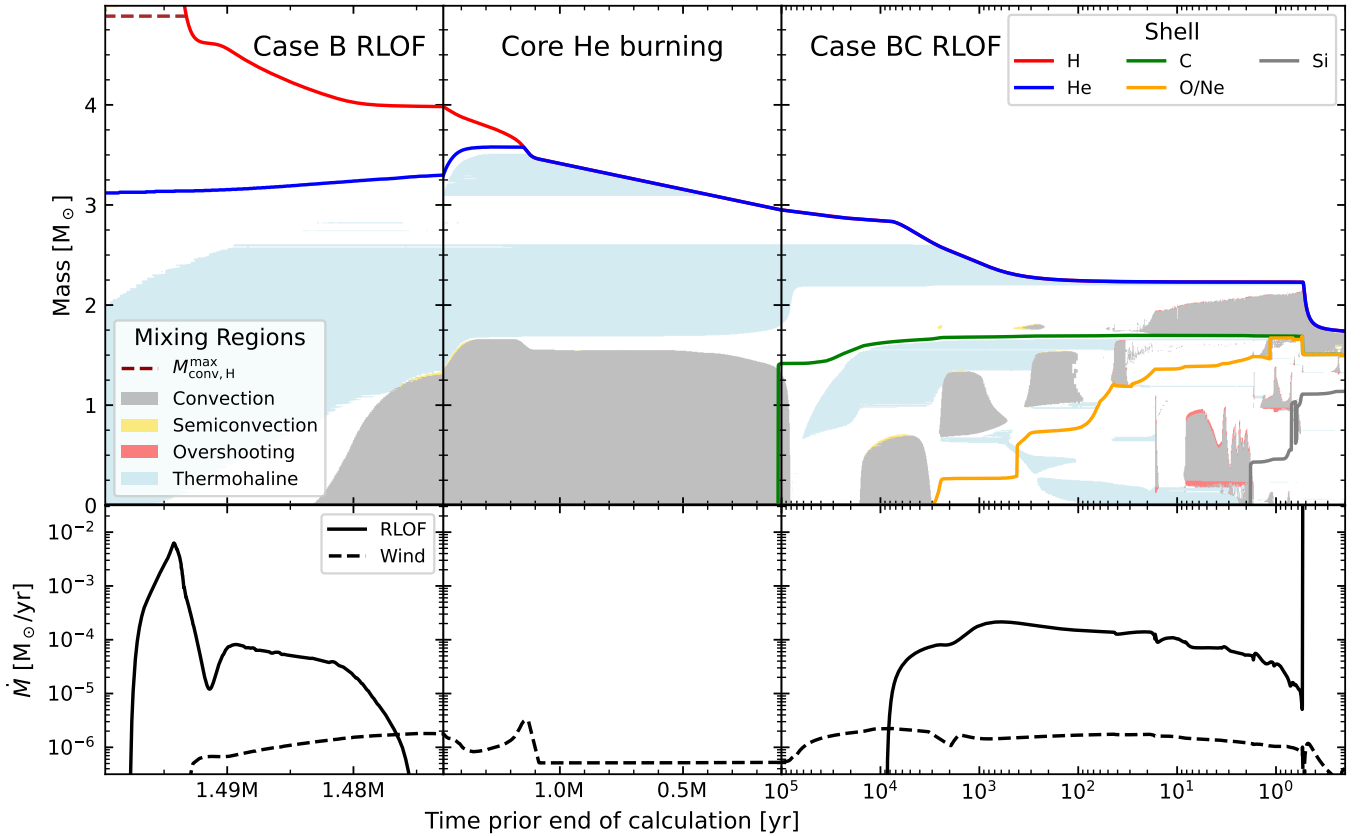


Fig. 4. Time evolution of the primary star in model $M_{1,i} = 13.5 M_{\odot}$, $q_i = 0.50$ and $P_i = 6.3 \text{ d}$ from the onset of Case B RLOF (left), during core He burning (center), and until the end of the run (right). Top: Kippenhahn diagram in which the outermost boundaries are colored corresponding to the most abundant element just below (see legend on the right) and colored patches based on the dominating mixing mechanism (see legend on the left). A dashed red line shows the maximum extent of the convective H-burning core during the MS. Bottom: Mass transfer rate (solid) and wind mass loss rate from the primary (dashed).

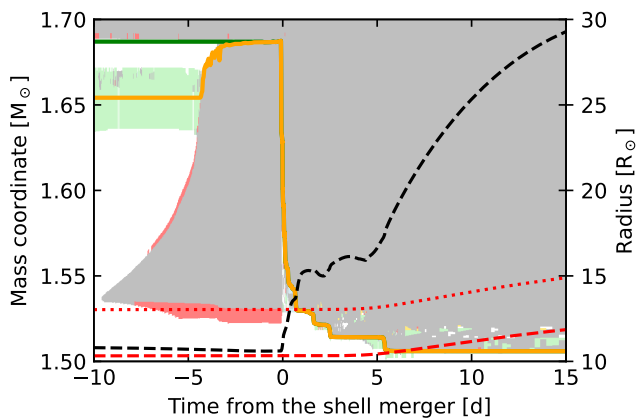


Fig. 5. A zoom in on the Kippenhahn diagram close to the CO/He shell boundary when the shell-merger event occurs. The solid lines, and patch colors are the same as in Fig. 4. The dashed lines correspond to the radius (black, dashed), the Roche lobe radius (red, dashed) and the volume-equivalent radius of the outer Lagrangian point (red, dotted).

Fig. 5). Additionally, ^{14}N is dredged down into the burning shell, triggering the chain $^{14}\text{N}(\alpha, \gamma) ^{18}\text{O}(\alpha, \gamma) ^{22}\text{Ne}(\alpha, n) ^{25}\text{Mg}$ which

releases free neutrons and likely initiates s-process nucleosynthesis.

The abrupt expansion triggers a new phase of mass transfer, which we will refer to as Case X RLOF¹. The resulting overflow ($R/R_{\text{RL},1} \approx 3$) is enough to engulf the companion, thus initiating a CE-phase. The model sheds $0.60 M_{\odot}$ during Case X RLOF, though this is a lower-bound estimate as mass transfer was ongoing at rates of $\geq 0.1 M_{\odot} \text{ yr}^{-1}$ when the model terminated. The SN-progenitor would retain a low-mass ($< 0.13 M_{\odot}$), metal rich ($\langle Z \rangle > 0.5$) envelope. With an orbital period of 8 d before Case X RLOF, the remaining time left to CC suggests the primary will likely explode during CE-evolution.

4.2. Overview

The binary models rerun in this work evolve similarly to the model in Sect. 4.1. Here, we now discuss the quantitative differences and trends, in the model grid. Each model is labeled ‘B’ followed by its initial mass and a letter denoting the initial orbital period. For example, B13.5b refers to the model with

¹ This is referred to as ‘late-stage’ mass transfer in WF22 or Case BBB RLOF in Tauris et al. 2013. We use a different nomenclature to highlight this phenomenon’s uncertain and extreme nature.

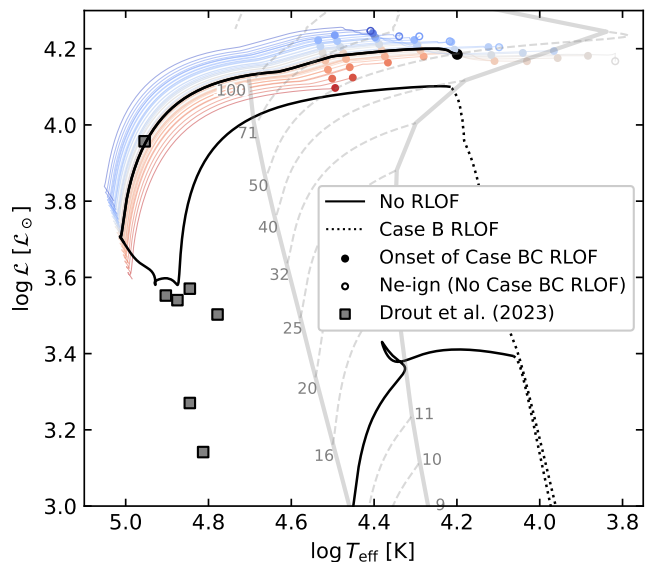


Fig. 6. The spectroscopic HR-diagram of the binary-stripped models explored in this work, color-coded by the mass at core He-depletion $M_{\text{He-dep}}$ (cf., Fig. 2). Each track is plotted from the end of core He-burning until the onset of Case BC RLOF (filled circle). For those that do not undergo RLOF, the plot is shown until the point found at 20yr before the end of the run (empty circle). The track of model B13.5b is highlighted in black and shown from ZAMS. The observed He-stars in the SMC by Drout et al. (2023) are also shown (black squares).

$M_{1,i} = 13.5 M_{\odot}$ and the second initial orbital period in the set, which is 6.3d, discussed in Sect. 4.1.

4.2.1. Case B RLOF and envelope loss

All the models in this set undergo Case B RLOF as the first mass transfer event, removing about $\sim 90\%$ of the primary’s envelope mass and leaving behind between 0.55 and 0.83 M_{\odot} of the H-rich envelope. This phase of mass transfer is stable in all models per our stability criterion (cf. Sect. 2.4).

After the onset of core He-burning, the remaining H-rich envelope is lost via shell burning and winds within 20% to 70% of the core He-burning lifetime. By the end of core He-burning, models with the same initial masses evolve into HeSs of varying masses (cf. Table. 2). Losing the H-rich envelope after a significant fraction of the core He-burning phase introduces some differences in the internal structure between single HeS and binary-stripped HeS models, discussed in Appendix C.

Observationally, the models align in the sHR diagram as a function of their core mass (cf. Fig. 6). The phase of core He-burning, while long-lived ($\sim 1.2\text{--}1.8$ Myr), is challenging to observe, particularly in the optical, due to the strong flux from the higher-mass MS companion. Recent UV observations by Drout et al. (2023) reveal HeS companions to otherwise apparently single MS stars exhibiting UV-excess. Some of their observed stars may evolve similarly to our models, depending on the mass and distance of the MS companion.

4.2.2. Case BC RLOF

All but the widest models in the set undergo Case BC RLOF after core He depletion. Although the majority of the models crashed before reaching CC (see Sect. 4.3), the bulk of the mass

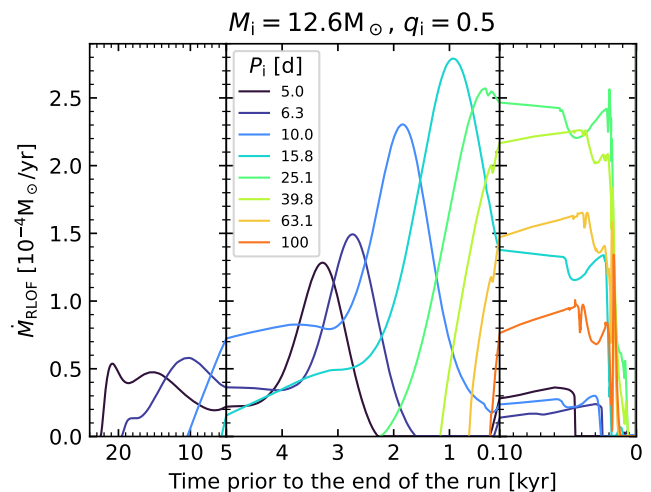


Fig. 7. Mass loss as a function of time prior to the end of the run for the set of models with $M_{1,i} = 12.6 M_{\odot}$ with different initial orbital period, marked by different colors. The three different panels highlight different time scales.

transferred during Case BC has been captured due to the limited mass transfer rates and the short time remaining before CC. This phase of mass transfer is stable for all models.

The time evolution of the mass transfer rate (cf. Fig. 7) depends on when RLOF begins. Generally, two phases can be distinguished. A weaker phase ($\dot{M}_{\text{RLOF}} < 10^{-4} M_{\odot} \text{ yr}^{-1}$) occurs > 5 kyr before CC, and is seen only in the tight systems starting RLOF much earlier. A stronger phase follows, as the envelope expands after the first C-burning shell ignites (between 6 kyr and 1 kyr before CC, depending on mass, cf. Fig. 1), leading to mass-transfer rates of up to $3 \times 10^{-4} M_{\odot} \text{ yr}^{-1}$. For the systems starting RLOF only in their last 5 kyr, \dot{M}_{RLOF} reaches high rates in the final ~ 100 yr before CC. In contrast, those already undergoing RLOF at this time show significantly lower rates closer to CC, and in some cases even detach. For all but the most massive models, mass transfer will terminate $\sim 20\text{--}40$ yr before CC, following the ignition of Ne.

Figure 8 shows that the mass-loss during Case BC ($\Delta M_{\text{RLOF-BC}}$) scales with how early the star is expected to fill its Roche lobe, determined by comparing the models’ Roche lobe radius with the radius of single HeS models of the same initial mass. Trends in $\Delta M_{\text{RLOF-BC}}$ align more closely to the single HeS radius evolution when compared using a variable other than $M_{\text{He-dep}}$ (cf. Appendix C). Mass lost during Case BC RLOF depends on early the model began RLOF, independently of the HeS mass (cf. Fig. 8 and Fig. C.2). If RLOF begins 20 kyr, 10 kyr, 5 kyr and 1 kyr before CC, it removes about 0.8 M_{\odot} , 0.6 M_{\odot} , 0.4 M_{\odot} and 0.1 M_{\odot} respectively. The stripping only affects regions of the envelope that are still rich in N.

4.2.3. Case X RLOF

This phase of mass transfer, previously outlined in Sect. 4.1.3, affects only half of the models, all of which fail to reach CC. Case X RLOF typically reaches mass loss rates of $10^{-2}\text{--}1 M_{\odot} \text{ yr}^{-1}$, removing 0.2 – 1 M_{\odot} of material. These values are lower-limits, as the models terminate before CC. Case X RLOF is always unstable as all models undergo OLOF and, in some cases, the HeS expands enough to engulf the secondary star.

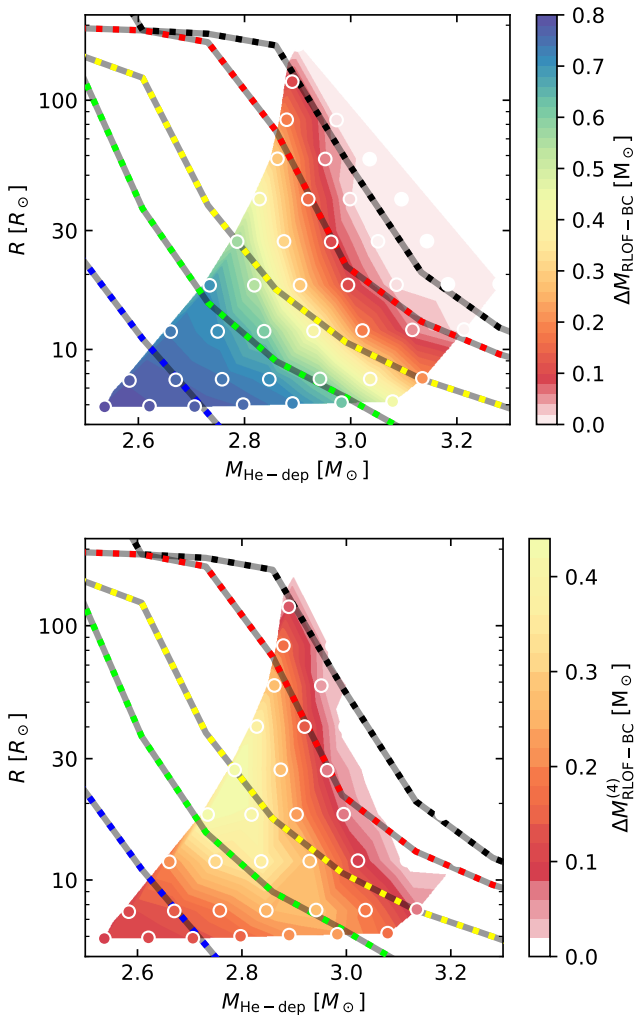


Fig. 8. Maps showing the $\Delta M_{\text{RLOF-BC}}$ (top) and the amount lost after \dot{M}_{RLOF} exceeds $10^{-4} M_{\odot} \text{ yr}^{-1}$ (i.e., $\Delta M_{\text{RLOF-BC}}^{(4)}$, bottom) in the $M_{\text{He-dep}} - R_{\text{RL},1}$ diagram. The scatter highlight the models, and the map is linearly interpolated between them. The dashed curves correspond to the radii of single HeS models as a function of mass at different times before the end of the run (20 kyr in blue, 10 kyr in green, 5 kyr in yellow, 1 kyr in red and 1 yr in black, cf. Fig. 2)

Case X RLOF typically begins after the onset of radiative Si-burning, and occurs in models exhibiting He-ingestion in the outer core. This ingestion leads to the increase in the luminosity of the star as well as the envelope opacity, causing the sudden expansion (cf., Sect. 4.1.3). However, there are some models which exhibit He-ingestion without expanding. The reason as to why helium is ingested in the first place remains uncertain.

Convective over- and undershooting likely play a key role in this phenomenon, (see Appendix D). These methods lack physical backing and were introduced to help convergence in the calculations. Consequently, we limit our discussion of the effects of Case X on the SN in detail to a more qualitative analysis (see WF22 for a detailed analysis of this phase of RLOF in HeS+NS binaries). To exclude the effects of He-ingestion and Case X RLOF, we use the pre-SN data at 1 yr before the model termination in subsequent sections.

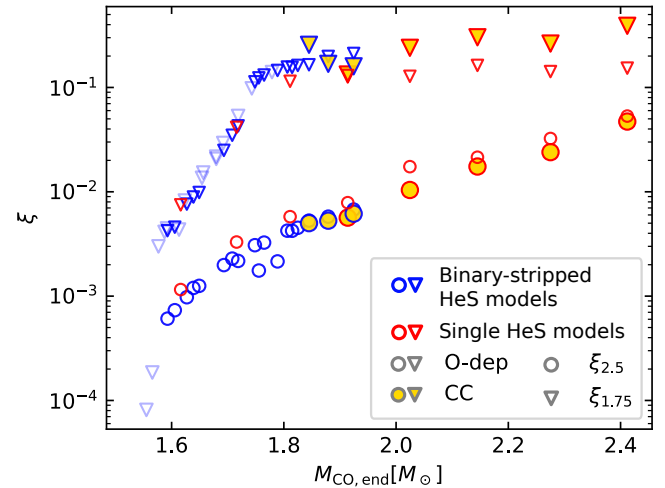


Fig. 9. Scatter plot showing the compactness parameter $\xi_m = (m/M_{\odot})/(R(m)/1000 \text{ km})$ for $m = 1.75 M_{\odot}$ (triangle marker) and $2.5 M_{\odot}$ (circle marker) as a function of the final CO-core. The results of both the single (red) and binary-stripped HeS models (blue) are shown. The compactness is evaluated at core O-depletion for all models (empty markers), including at CC for those that reached it (gold fill). Models with $M_{\text{end}} < 2.5 M_{\odot}$ are shown with lighter colors.

4.3. Termination and Explosion Properties

The majority of our models develop a Si-rich core, and only three (B13.8d, B14.1c, and B14.1d) reach the point of CC. These models provide estimates for the time between CC and specific burning phases: 22 – 10 yr after core Ne-burning, 10 – 1 yr after core O-burning, and about 10d after core Si-burning.

Models B12.3a-e, B12.3j and B12.6a-b terminate while burning Ne/O off-center. Of these, B12.3a (the most-stripped model) exhibits central density and temperature evolution akin to that of a ECSN progenitor (cf. Sect. 3.1 and Tauris et al. 2015). All other models display higher temperatures, indicating that they will eventually undergo CC.

We apply the prescriptions from Müller et al. (2016) and Mandel & Müller (2020) to the models reaching CC, and obtain explosion energies of $E_{\text{kin,ej}} = 5.8 - 7.0 \times 10^{50}$ erg, nickel-masses of $M_{\text{Ni}} = 0.03 - 0.04 M_{\odot}$ and NS masses of $M_{\text{ns}} = 1.34 - 1.37 M_{\odot}$. These values resemble those reported in Ertl et al. (2020) based on the HeS models from Woosley (2019). We investigate the compactness parameter ξ_m (O’Connor & Ott 2011; Sukhbold & Woosley 2014) of our models at the end of the run (cf. Fig. 9), and find that $\xi_{2.5}$ decreases with decreasing $M_{\text{CO,end}}$. This trend aligns with previous studies (e.g., Ertl et al. 2020; Aguilera-Dena et al. 2022, 2023) where also $E_{\text{kin,ej}}$ also decreases to as little as $1.0 - 1.2 \times 10^{50}$ erg. Since all these values are derived from recipes based on 1D-explosion models, they may be uncertain, and we also consider other values for the explosion energy and nickel mass below.

In the following sections, we adopt a mass $M_{\text{ns}} = 1.35 M_{\odot}$ for the NS, and discuss the effects of the adoption of other values between $1.20 M_{\odot}$ and $1.50 M_{\odot}$. The ejecta mass of the resulting SNe is given by $M_{\text{ej}} = M_{\text{end}} - M_{\text{ns}}$. The composition of the ejecta is also noted, and it is distinguished between He and metals ($M_{\text{ej}}(\text{He})$ and $M_{\text{ej}}(\text{Z})$ respectively), as shown in Fig. 10.

Except for the most heavily stripped models, the ejecta is He-rich (Fig. 10), and we can therefore assume that these will explode as Type Ib SNe. However, simulations of the explosion

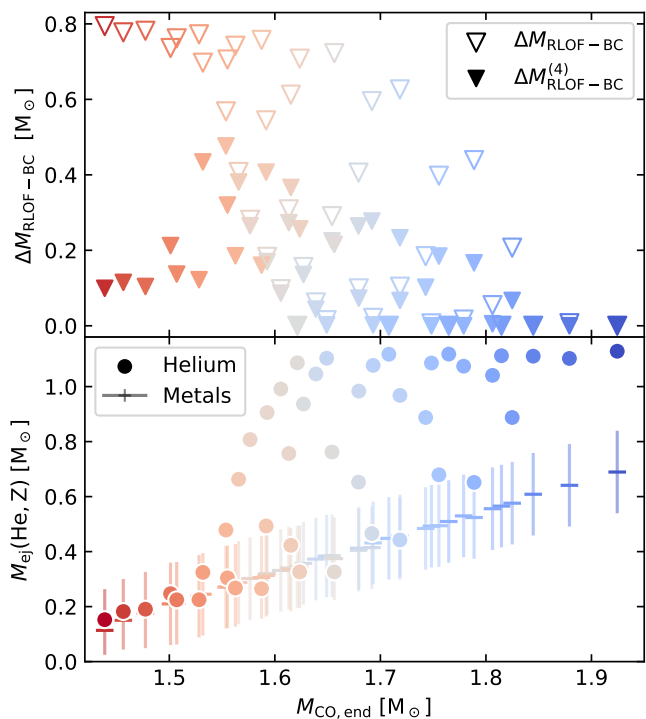


Fig. 10. Properties of the primaries as a function of the final CO-core mass of the primary star. The markers are colored as a function of $M_{\text{He-dep}}$, as in Fig. 2. Top: Amount of mass ejected during Case BC RLOF. The empty markers represent the total mass lost via mass transfer, while the filled markers represent the mass shed during mass transfer after $\dot{M}_{\text{RLOF}} > 10^{-4} M_{\odot} \text{ yr}^{-1}$ for the first time. Bottom: The amount of helium (circles) and metals (error bars) found in the ejecta. The uncertainty in the metal content derives from assuming M_{ns} to be within $0.15 M_{\odot}$ of the fiducial value (horizontal marker).

of low-mass HeS models show peculiar nebular spectra, which do not at present have any observational counterparts (Dessart et al. 2021, 2023). One possible explanation is that they instead lead to Type Ibn SNe (Dessart et al. 2022). The average He content in the ejecta varies significantly depending on the CO-core mass and the degree of stripping. The least massive models at CC ($M_{\text{end}} < 2.1 M_{\odot}$) have comparable amounts of He and metals in the ejecta, within a reasonable deviation of M_{ns} from its fiducial value. The transition to a Type Ic SN also depends on the details of the explosion (e.g. the degree of mixing of Ni in the He-rich regions, as well as asymmetries in the explosion itself, would affect the excitation of HeI lines, Lucy 1991; Dessart et al. 2012; Woosley et al. 2021). More stripped models, with low He and high metal abundances in their ejecta, are more likely to explode as Type Ic SNe.

While we will solely focus on the CSM interaction features of the SN in later sections, we also outline the effects of the newly-born NS on the SN and the ejecta-companion interaction in Appendix E.

4.4. Post-SN evolution of the system

Following the SN, intense mass-loss and natal-kicks on the newly-born NS, (Burrows et al. 1995; Janka 2017) affect the orbital evolution of the system, increasing its eccentricity and even unbinding it. The overall low-mass of the SN progenitors may result in a lower natal kick (Janka 2017). Combined with the

relatively short pre-explosion orbital periods, this increases the probability of these systems remaining bound, potentially forming a Be-X-ray binaries (cf. Sect. 4.1.1).

The secondary is expected to evolve much like a single star until it is close to filling its Roche lobe. Here, mass transfer will likely turn unstable, triggering a CE-phase. If the CE is ejected, a tight WD+NS binary may form. Conversely, if the CE is not ejected, the NS will merge with the companion forming a Thorne-Żytkow object. These results can also be extended to systems with more massive secondaries than those presented here (cf. Appendix B). In such cases, the CE-phase may produce a tight HeS+NS binary, where the HeS is massive enough to undergo CC. The resulting SN explosion could exhibit interacting features if Case BC RLOF occurs between the HeS and its NS companion (e.g., WF22). If the natal kick of the newly-formed NS does not disrupt the binary, the system forms a double-NS system, which would eventually merge and emit gravitational waves (Qin et al. 2024).

5. Supernova-CSM interaction

All SN-progenitor models that undergo Case BC RLOF explode with a significant amount of H-poor material likely remaining close to the binary system. Here, we discuss the CSM properties from our models (Sect. 5.1 and 5.2), their potential effects on the SN light curve (Sect. 5.3-5.5) and a discussion on the number of interacting H-poor SNe expected from binary models (Sect. 5.6). We do not pursue a discussion of the effect of the CSM on the spectral evolution (but see Dessart et al. 2022), as this depends on strongly non-linear physics and requires detailed radiative-transfer modeling.

5.1. CSM mass

The upper limit on the CSM mass (M_{CSM}) in our models is given by $\Delta M_{\text{RLOF-BC}}$. Some of this mass may escape the system and therefore not affect the SN. Most observations do not track the late-time evolution of the SN, often missing out on the prolonged interaction phase (e.g., Type IIn SNe, Smith et al. 2017). This restricts inferred CSM properties to the closer, denser regions where interaction power dominates the observed light-curve.

Our models constrain the total mass lost from the binary but are less predictive of the circumbinary density distribution. To exploit the time-evolution of the mass outflow from the binary model, we compute not only its total amount but separately also the amount of mass that was lost during the stronger phase of mass transfer in the last $\lesssim 3$ kyr before CC (cf. Fig. 7), as

$$\Delta M_{\text{RLOF-BC}}^{(4)} = \int_{t_4}^{t_{\text{CC}}} \dot{M}_{\text{RLOF}} dt, \quad (1)$$

where t_4 is the time during Case BC RLOF such that \dot{M}_{RLOF} exceeds $10^{-4} M_{\odot} \text{ yr}^{-1}$ for the first time. This quantity is not sensitive to the adopted threshold (see Fig. 7). Unlike $\Delta M_{\text{RLOF-BC}}$, $\Delta M_{\text{RLOF-BC}}^{(4)}$ does not correlate with the time the star fills its Roche lobe. Systems that undergo RLOF exclusively within 10 kyr before CC achieve the highest values of $\Delta M_{\text{RLOF-BC}}^{(4)}$ (cf. Fig. C.2, and Sect. 4.2.2), and those that begin RLOF even later ($\lesssim 3$ kyr before CC) lose all their mass at high rates, resulting in $\Delta M_{\text{RLOF-BC}}^{(4)} \simeq \Delta M_{\text{RLOF-BC}}$ (cf. Fig. 7).

In Fig. 11, we find a strong anticorrelation between M_{ej} and M_{CSM} when assuming $M_{\text{CSM}} = \Delta M_{\text{RLOF-BC}}$, which is also present when we extrapolate $\Delta M_{\text{RLOF-BC}}$ in the whole BG set.

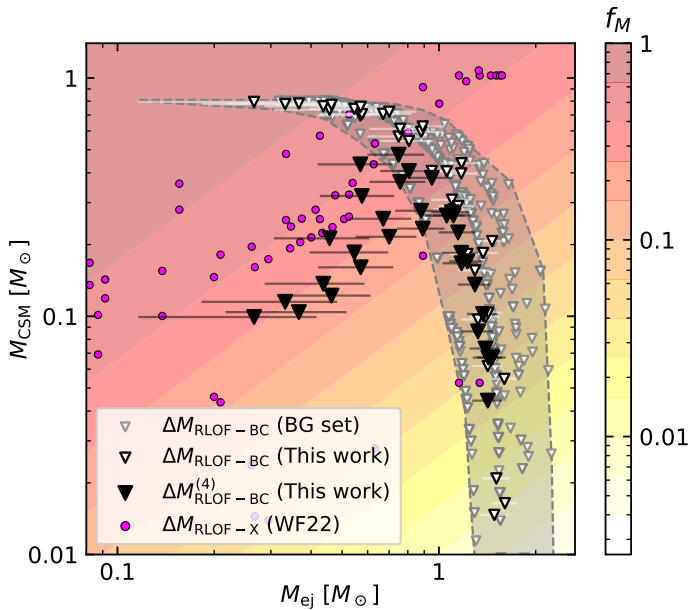


Fig. 11. The CSM in our models at the time of the SN, according to various estimates, versus the SN ejecta mass. The CSM mass given by $\Delta M_{\text{RLOF-BC}}$ (white, with black outline) and $\Delta M_{\text{RLOF-BC}}^{(4)}$ (black) is shown. CSM mass estimates for models in the BG set are given as smaller white triangles with gray rim, and the region occupied by these models is shaded in gray. The results from the models in WF22 are shown as magenta dots. The background colormap represents the estimated maximum conversion fraction of kinetic energy into radiation via CSM interaction (f_M , Eq. (2))

This extrapolation is done by mapping each model in the BG set onto Fig. C.2 and assuming $M_{\text{ns}} = 1.35 M_{\odot}$. This anticorrelation is driven by the fact that the lower-mass models expand more and therefore lose more mass (cf. Sect. 4.2.2 and Fig. 8) compared to higher-mass models. The combinations of M_{CSM} and M_{ej} result in different effects on the light-curve (background color, Fig. 11) which will be discussed in Sect. 5.3.

When assuming $M_{\text{CSM}} = \Delta M_{\text{RLOF-BC}}^{(4)}$, trends differ only for $M_{\text{ej}} < 1 M_{\odot}$, where M_{CSM} decreases with decreasing M_{ej} (cf. Fig. 11). This is because, even though lower mass models generally lose more mass, the absolute amount lost in the last 5 kyr is proportionally much less than in other systems (cf. Fig. 7 and the bottom panel in Fig. 8).

5.2. CSM extension and shape

As we do not model the CSM density structure, we estimate its spatial extension analytically under simple assumptions. For this, we consider two approaches.

In the first approach, we assume that the CSM consists of a steady spherical outflow with constant velocity v_{CSM} , from which we can infer its extent. For $v_{\text{CSM}} = 10 \text{ km s}^{-1}$, the CSM would extend to distances of $10^{15} \sim 10^{18} \text{ cm}$ (cf. Fig. 12). These distances correlate with the mass of the CSM, with the more extended CSM containing more mass (cf. Sect. 4.2.2). Most of our mass donors detach from their Roche lobe before CC (except those with $M_{\text{He-dep}} > 2.90 M_{\odot}$ and $R_{\text{RL}} < 30 R_{\odot}$), usually by core Ne-ignition. This leaves a cavity, extending to $\sim 6 \times 10^{14} \text{ cm}$, filled by donor’s stellar wind. In models that do not detach, mass transfer in the last $\sim 20 \text{ yr}$ deposits $\sim 0.001 M_{\odot}$ of material in that region (Fig. 12).

Alternatively, material that leaves the binary may accumulate in a circumbinary disk (CBD), if channeled through the outer Lagrangian point of the accretor (e.g., Lu et al. 2023). Whether or not the material remains bound depends on its velocity. Given the high mass-ratio of the systems during Case BC RLOF, material escaping from the outer Lagrangian point with a small perturbation may remain gravitationally bound, feeding the disk. The inner disk radius is expected to be comparable to two to three times the semi-major axis of the binary (Artymowicz & Lubow 1994; Pejcha et al. 2016), corresponding to $10^{13} - 10^{14} \text{ cm}$ in our models. The outermost disk radius is limited by photoevaporation from the radiation emitted by the stars in the inner binary (Hollenbach et al. 1994). For a post-CE binary with $M_1 = M_2 = 10 M_{\odot}$ in a tight orbit with $a = 30 R_{\odot}$ and a CSM of $1 M_{\odot}$, Tuna & Metzger (2023) find that the CBD extends up to $3000 \sim 10000 R_{\odot}$ (cf. their Eq. 29 and Fig. 5), i.e., about $100 - 300$ times the orbital separation. Adopting the conservative value of $100a$ as the outermost edge of the disk, we estimate CBDs in our models to extend between $6 \times 10^{12} \text{ cm}$ and $4 \times 10^{15} \text{ cm}$ (cf. Fig. 12).

We can extend this consideration to the BG set of binary models. Final orbital separation for systems undergoing Case BC RLOF are derived by estimating $\Delta M_{\text{RLOF-BC}}$ (see Sect. 5.1) and integrating Eq. (5) in Willcox et al. (2023) for each candidate model. The resulting CBDs are expected to extend between $3 \times 10^{12} \text{ cm}$ and 10^{16} cm .

5.3. Cumulative effect on the light-curve

As the expanding ejecta collide with the CSM, a fraction of its kinetic energy will be converted into radiation, thus affecting the SN light curve. Type Ibc SNe show a total radiated energy of $\lesssim 10^{49} \text{ erg}$ (Nicholl et al. 2015). For an explosion energy $E_{\text{kin,ej}}$ of $6 \times 10^{50} \text{ erg}$ (cf. Sect. 4.3), CSM interaction could dominate the typical Type Ibc light curve more than $\sim 2\%$ of the kinetic energy is converted into light. For $E_{\text{kin,ej}} = 10^{50} \text{ erg}$, more than 10% of $E_{\text{kin,ej}}$ would need to be converted.

Assuming an inelastic collision, the cumulative interaction power can be estimated as (Aguilera-Dena et al. 2018)

$$E_{\text{rad}} = \eta E_{\text{kin,ej}} f_M f_v^2, \quad (2)$$

where η is the efficiency with which kinetic energy is converted into radiation, and the two multiplicative factors represent the mass ($f_M = \frac{M_{\text{CSM}}}{M_{\text{ej}} + M_{\text{CSM}}}$) and velocity ($f_v = \frac{v_{\text{ej}} - v_{\text{CSM}}}{v_{\text{ej}}}$) contrasts between the ejecta and the CSM. Assuming that the CSM is slow-moving ($f_v \sim 1$), and that the conversion is highly efficient ($\eta \sim 1$), the fraction of kinetic energy converted into radiation equals f_M , which is only a function of the ejecta mass and the CSM mass.

The value of f_M increases with decreasing ejecta mass and increasing CSM mass (cf. Fig. 11), peaking in the models with the most stripping (~ 0.75 if $M_{\text{CSM}} = \Delta M_{\text{RLOF-BC}}$, and ~ 0.45 if $M_{\text{CSM}} = \Delta M_{\text{RLOF-BC}}^{(4)}$). Models with less stripping during Case BC RLOF, can still convert as much as 10% of $E_{\text{kin,ej}}$ into radiation if $M_{\text{CSM}} > 0.1 M_{\odot}$. For both cases, interaction would convert a significant fraction of the SN kinetic energy into radiation, strongly impacting the SN light curve.

The low mass-loss rates in our models imply low CSM densities, meaning the SN radiation may not thermalize and therefore not result in an optically-luminous transient. Instead, most of the flux would come out in the UV or as X-rays (Dessart & Hillier 2022). Consequently, we focus on the case in which the CSM

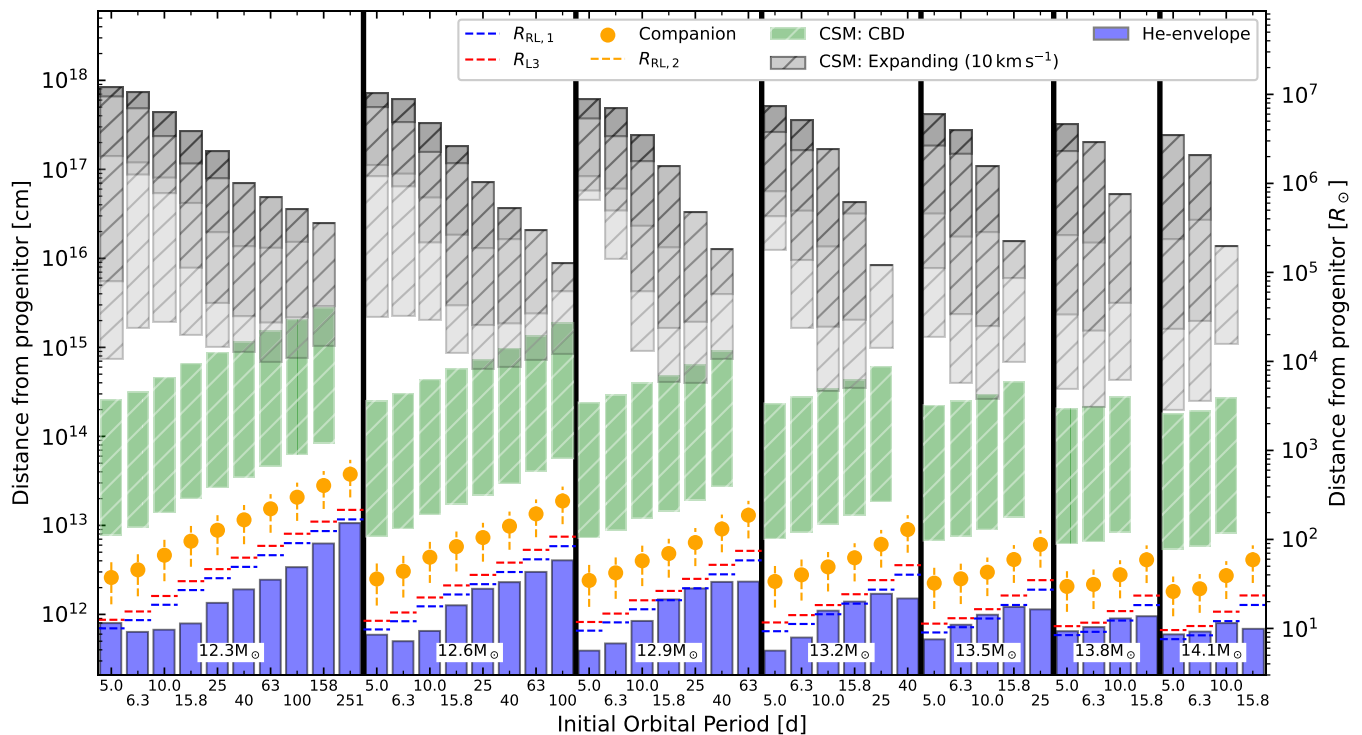


Fig. 12. Bar chart of the spatial distribution of material from the SN progenitor models 1 yr prior to the end of the run for the models run in this work. Color bars highlight the envelope (blue filled bar) and the regions where the CSM would be found (hatched bars) if it were distributed along a CBD (green) or if it were expanding isotropically, at a constant speed of 10 km s^{-1} (gray). In the latter case, the minimum radius is set as the point where the cumulative mass of the CSM from the progenitor star reaches $0.001 M_{\odot}$, and increases in contrast when it reaches 0.01 , 0.1 and $0.5 M_{\odot}$. The Roche lobe radius of the progenitor star is shown (blue hatched-line) as well as the volume-equivalent radius of the outer Lagrangian point (red hatched-line). Finally the companion’s location is also shown (yellow marker) alongside its Roche lobe (vertical yellow hatched-line). The models are grouped by different initial masses (indicated in the bottom of each box).

is distributed along a CBD, where higher densities are achievable. We consider isotropically expanding ejecta impacts a CSM confined within a half-opening angle θ from the orbital plane. The effective ejecta mass $M_{\text{ej,eff}}$, that is the part of the ejecta that will impact the CSM, is smaller than the total amount M_{ej} and is determined by the solid angle that the CSM subtends:

$$\frac{M_{\text{ej,eff}}}{M_{\text{ej}}} = \frac{\int_0^{2\pi} d\varphi \int_{-\theta}^{\theta} \cos \alpha d\alpha}{4\pi} = \sin \theta. \quad (3)$$

Recalculating the energy lost due to the inelastic collision, we obtain a similar form to Eq. (2), with

$$f_M(\theta) = \sin \theta \left(1 + \frac{M_{\text{ej}} \sin \theta}{M_{\text{CSM}}} \right)^{-1}. \quad (4)$$

For $M_{\text{ej}} \sim M_{\text{CSM}}$ and $\theta \ll 1$, then $f_M(\theta) \sim \theta$. The cumulative interaction-power will exceed the typical radiated energy in Type Ibc SNe as long as $\theta > 1^\circ$ for $E_{\text{kin,ej}} = 6 \times 10^{50} \text{ erg}$, or $\theta > 5.5^\circ$ for $E_{\text{kin,ej}} = 10^{50} \text{ erg}$. Even for very thin disks, interaction power can dominate the cumulative radiation. In thin disks, high densities may trap radiation, causing it to expand the material rather than escape as radiation. Consequently, our estimates represent upper-limits on radiated energy.

Below, we consider at which time the light curve might be affected the most, based on different assumptions on the CSM structure.

5.4. Interaction light-curve for a constantly expanding CSM

We present simplified light curve models, assuming interaction as the sole source of SN luminosity. We neglect diffusion processes and the spatial extension of the ejecta and the swept-up CSM, and focus on the conversion rate of kinetic energy into escaping radiation. The equations are detailed in Appendix F.1.

We use model B12.3e as our fiducial model, as it shows the strongest mass-loss rate close to CC of all models ($3.1 \times 10^{-4} M_{\odot} \text{ yr}^{-1}$). The results are shown in Fig. 13. We also assume that the CSM is isotropically distributed.

The interaction luminosity (L_{inter}) becomes significant only after a few days, due to the presence of the cavity in the CSM (Sect. 5.2) which would otherwise be filled by winds which are presently ignored. The light-curve also exhibits a plateau after the onset of the interaction, which is qualitatively similar to that obtained in detailed radiative-transfer models in Dessart et al. (2022) for a wind-like CSM. This plateau, which is not usually present in most observed Type Ibn SNe with the exception of OGLE-2012-SN-006 (Pastorello et al. 2015a), arises from the roughly constant mass-loss rate. The ejecta therefore sweep about the same amount of mass per unit time, producing a steady energy conversion rate. The absence of diffusion processes in the model is also gives rise to this peculiar signal, as its inclusion would have altered the luminosity evolution at early times, where the CSM is denser and more optically thick.

The effect of varying v_{CSM} are shown in Fig. 13. Higher v_{CSM} increases the lag time before the onset of interaction and decreases L_{inter} (cf., Eq. F.9) and vice-versa. The interaction per-

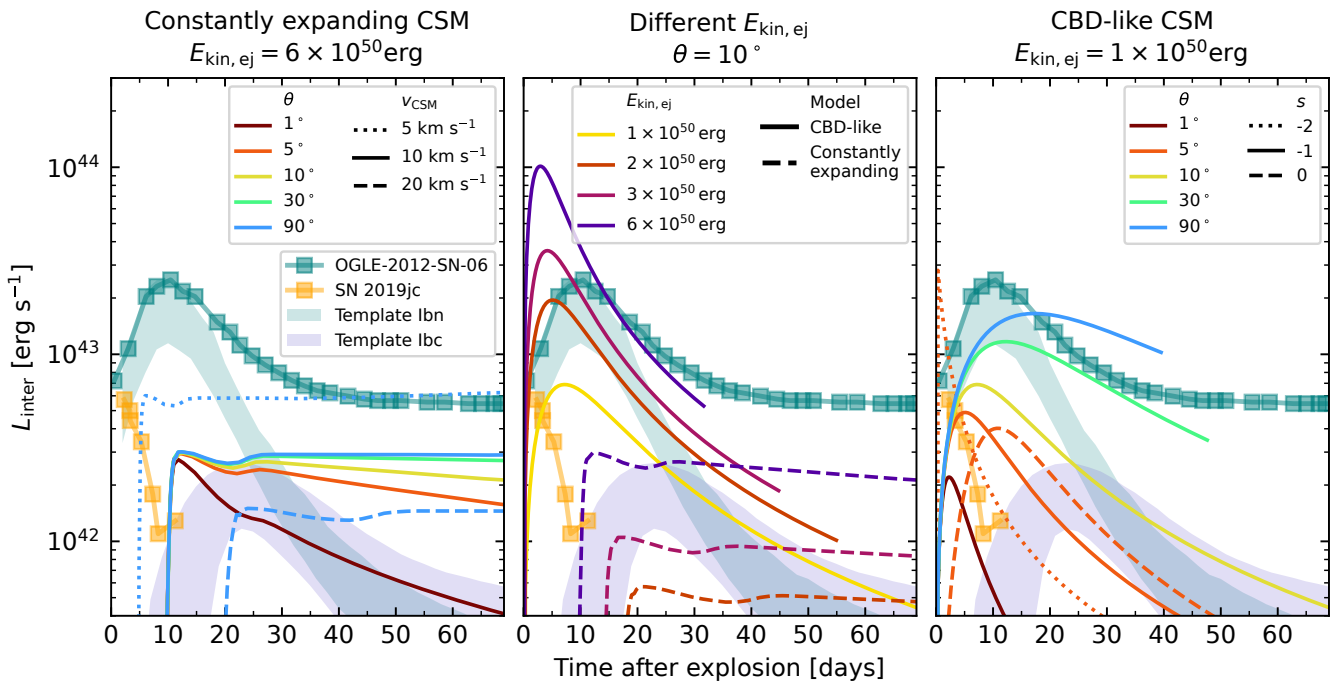


Fig. 13. Interaction-powered light curves for model B12.3e assuming a constantly-expanding CSM (left panel), a CBD-like CSM (right panel), and a comparison between the two with different explosion energies (center panel). In each panel, two observations are shown, namely the Type Ibn SN OGLE-2012-SN-006 (Pastorello et al. 2015a, light-blue scatter), and the Type Icn SN 2019jc (Pellegrino et al. 2022a, orange scatter) as well as the template light curves for Type Ibc SNe (Nicholl et al. 2015, in violet, where the peak is located at the same time as in the light-curve of model he4 from Dessart et al. 2020) and Type Ibn SNe (Hosseinzadeh et al. 2017, in blue, where the peak is arbitrarily placed at 10 d). Left: the CSM is assumed to constantly expand at $v_{\text{CSM}} = 10 \text{ km s}^{-1}$, with different opening angles (with different colors) and with $E_{\text{kin,ej}} = 6 \times 10^{50} \text{ erg}$. For $\theta = 90^\circ$, models with v_{CSM} of 5 km s^{-1} (dotted line), and 20 km s^{-1} (dashed line) are also shown. Center: interaction power from the CBD-like CSM (solid, with $R_{\text{in}} = 10^{13} \text{ cm}$, $R_{\text{out}} = 10^{15} \text{ cm}$ and $s = -1$) and constantly expanding CSM (dashed, with $v_{\text{CSM}} = 10 \text{ km s}^{-1}$) are shown with different $E_{\text{kin,ej}}$ (different colors), assuming an opening angle $\theta = 10^\circ$. Right: the CSM is assumed to be CBD-like, with $R_{\text{in}} = 10^{13} \text{ cm}$, $R_{\text{out}} = 10^{15} \text{ cm}$, $s = -1$ and different opening angles (different colors). For $\theta = 5^\circ$, the cases with $s = 0$ (dashed) and $s = -2$ (dotted) are also shown.

sists for as long as several years, as the ejecta sweeps material that has travelled since the beginning of Case BC RLOF. However, the optical signal will remain weak and likely become undetectable much earlier than that, as only the innermost CSM is optically thick.

An aspherical CSM distributed along a torus, confined near the orbital plane within a half-opening angle θ , presents a more interesting scenario. Here, only a fraction of the ejecta interacts with the CSM ($M_{\text{ej,eff}}$, cf. Sect 5.3), which decreases with smaller θ . At the onset of interaction L_{inter} remains unaffected, as the same amount of mass would be swept up independently of θ . However, smaller θ cause a stronger deceleration of the effective ejecta, reducing L_{inter} at later times (see Eq. F.9). Significant effects arise only for very small opening angles ($< 10^\circ$).

Lower $E_{\text{kin,ej}}$ affect the light-curve in two ways, due to the slower expanding ejecta: reduced luminosity and delayed onset of interaction (cf. Fig. 13). As in the model $L_{\text{inter}} \sim E_{\text{kin,ej}}^{3/2}$, the overall luminosity decreases strongly with decreasing $E_{\text{kin,ej}}$. The onset of interaction is instead delayed by a factor $v_{\text{ej}} \sim E_{\text{kin,ej}}^{1/2}$. For $E_{\text{kin,ej}} \leq 10^{50} \text{ erg}$, the interaction luminosity drops to $\lesssim 2 \times 10^{41} \text{ erg s}^{-1}$, and would remain largely undetectable.

5.5. Interaction light-curve for a CBD-like CSM

We now model the interaction assuming the CSM is a bound CBD (such that $v_{\text{CSM}} = 0$) rather than spherically symmetric (cf. Sect. 5.2). This approach introduces additional parameters and assumptions – such as the half-opening angle θ , the CBD density

profile and its radial extent – which are not constrained by our models. We will assume that $\rho(r) \sim r^s$, with $s \leq 0$, and that the CBD is confined between $R_{\text{in}} = 10^{13} \text{ cm}$ and $R_{\text{out}} = 10^{15} \text{ cm}$.

As a proof of concept, we present a simplified light curve model (see Appendix F.2), assuming $E_{\text{kin,ej}} = 10^{50} \text{ erg}$ (Fig. 13). The effect of varying θ is more pronounced than in the case of a constantly expanding CSM. For thinner disks, L_{inter} is weaker and dims faster, as less ejecta interacts with the CBD. The characteristic bell-shape feature, typical of many Type Ibn SNe (cf. Hosseinzadeh et al. 2017), is qualitatively reproduced. Varying s also has a considerable effect, as a steeper density profile (i.e., lower s) confine the CBD closer to the binary, resulting in an earlier interaction and higher initial L_{inter} (Fig. 13). Even when adopting such a low $E_{\text{kin,ej}}$, the interaction power is still significant even for $\theta = 5^\circ$ where L_{inter} peaks at $> 2 \times 10^{42} \text{ erg s}^{-1}$. Unlike the constantly-expanding CSM scenario, interaction terminates after $\sim 70 \text{ d}$, as the entire CBD is swept away.

Adopting $E_{\text{kin,ej}} > 10^{50} \text{ erg}$ results in a brighter and faster-evolving light-curve, similarly to the case of a constantly expanding CSM (cf. Sect. 5.4, and Fig. 13), as the peak brightness scales with $E_{\text{kin,ej}}^{3/2}$ and the peak time with $E_{\text{kin,ej}}^{1/2}$. Models with $\theta \geq 10^\circ$ are capable of exceeding the typical luminosity of Type Ibc SNe, even with $E_{\text{kin,ej}} < 10^{50} \text{ erg}$. This model can also qualitatively reproduce the behavior of Type Icn SN 2019jc, especially in the case of thin, confined CBD and higher $E_{\text{kin,ej}}$.

This experiment, while very crude, demonstrates that a disk-like CSM can significantly shape the light-curve, particularly for thin disks, which qualitatively match some observed Type Ibn and Type Icn light curves. This model however neglects radiation

transport, which would smear the interaction power on longer timescales, or even reduce the radiated energy if some is used to expand the material in the CBD. The interaction’s asymmetry introduces viewing angle effects. In the case of edge-on observations, the light-curve may be additionally smeared-out (see [Vlasis et al. 2016](#); [Suzuki et al. 2019](#), in the context of Type II SNe). Finally, a disk-like structure may conflict with the narrow-line emission spectra ([Smith 2017](#)).

5.6. Predicting the number of interacting H-poor supernovae

Since we infer the mass-loss during Case BC RLOF from each model in the BG set (cf. Sect. 5.1 and Fig. 11), we provide population estimates for the models we predict will develop into an interacting SN. As shown throughout Sects. 5.3-5.5, a significant fraction of the kinetic energy of the ejecta can be converted into radiation when $M_{\text{CSM}} \gtrsim 0.1 M_{\odot}$. We assume that an interacting H-free supernova may likely develop in those systems where the donor star underwent Case BC RLOF.

We assume that all stars are born in binaries, that the binary models that undergo unstable RLOF in the BG set will merge (see Sect. 2.4), and that the merger product will evolve like a single star of the same mass as the sum of the two component stars. Assuming a [Salpeter \(1955\)](#) initial-mass function and a flat initial P_i and q_i distribution, we obtain that up to 12% of all stripped-envelope SN progenitors in the BG set are potential progenitors of H-poor interacting SNe. The observed fraction of Type Ibn SNe reported in [Perley et al. \(2020\)](#) is 9.2%, although this is a magnitude-limited sample and therefore is biased towards more luminous events. This similarity suggests that binary mass transfer might be a suitable channel to create the majority of interacting H-free SNe.

6. Comparing observed interacting H-poor SNe with the models

To date, there is a growing number of H-poor SNe that exhibit features compatible with that of interaction with a nearby CSM. The light curve and the spectra provide insight into both the explosion parameters of the SN (M_{ej} , v_{ej} , M_{Ni} and $E_{\text{kin,ej}}$) and the properties of the CSM (M_{CSM} , R_{CSM}), albeit under a series of assumptions (see [MOSFiT](#), [Guillochon et al. 2018](#), and also [Chatzopoulos et al. 2012, 2013](#); [Villar et al. 2017](#)). These models typically assumed isotropic CSM distributions around the progenitor, with a density profiles of the form $\rho(r) \sim r^s$ starting at a distance R_{CSM} . Many works usually keep the parameter s fixed to either 0 (a constant distribution) or -2 (wind-like) or explore both, yielding significantly different light-curve fitting parameters (e.g., [Ben-Ami et al. 2023](#)). More recent theoretical works have produced Type Ibn SNe by exploding a low-mass He-star model while surrounded by a massive CSM, yielding interesting matches to the light curves and spectra of events like SN 2006jc, SN 2018bcc and SN 2011hw ([Dessart et al. 2022](#)).

There is a notable lack of systematic analysis of H-poor interacting SNe. Many studies incorporate additional physical processes, such as Ni-decay or magnetar spin-down, which complicate the interpretation of the effects of CSM interaction. Moreover, the discussion in Sect. 5.2 tells us that the CSM may be distributed aspherically, violating the assumption of isotropy used in standard light-curve fitting methods. These modeling uncertainties inevitably affect the interpretation of observations.

In this work, we compare our model predictions with published observationally-inferred properties of H-poor interacting

SNe, without making claims about any specific observed event. It should be emphasized that we use literature values without assessing their accuracy or robustness. Some of the values, especially from older studies, may be inaccurate.

We searched the literature for H-poor interacting SNe and included only those for which M_{CSM} values are available. In the following, we discuss Type Ibn SNe (Sect. 6.1) and Type Icn/Ic-CSM SNe (Sect. 6.2), while in Appendix G we discuss also other transients like USSNe and SLSNe.

6.1. Type Ibn SNe

The sample of Type Ibn SNe includes H-poor and He-rich transients that showcase narrow He-emission lines. The sample spans a wide range of M_{ej} (between 0.6 and $20 M_{\odot}$), and M_{CSM} (between 0.01 and $2 M_{\odot}$). Most SNe in the sample cluster around $M_{\text{ej}} \sim 1 M_{\odot}$ and M_{CSM} between ~ 0.1 and $1 M_{\odot}$. Despite their large uncertainties, these values align with the parameter space predicted by our models (cf. top-left panel of Fig. 14), regardless of whether M_{CSM} corresponds to $\Delta M_{\text{RLOF-BC}}$ or $\Delta M_{\text{RLOF-BC}}^{(4)}$. Some SNe fall outside of the predicted $M_{\text{CSM}} - M_{\text{ej}}$ region (SN 2006jc, SN 2010al, ASASSN-14ms, SN 2020bjj, SN 2019uo). These outliers, characterized by high M_{ej} , likely originate from a different evolutionary channel.

The typical inferred CSM extension for Type Ibn SNe exceeds 10^{14} cm (cf., Fig. 14, right panel), consistent with the CBD-like CSM expected from the models. Notable exceptions include SN 2020bjj, whose inferred CSM extent is similar to the radii of our SN-progenitor models, and SN 2006jc ($> 10^{16}$ cm), which appears to be instead in agreement with the case of a slow-moving CSM.

The majority of the Type Ibn SNe collected deviate from the Type Ibn template of [Hosseinzadeh et al. \(2017\)](#) as reflected in their the total radiated energy in the light-curve E_{rad} (cf., Fig. 14, bottom-left panel). Most SNe from [Hosseinzadeh et al. \(2017\)](#) lack M_{CSM} estimates and were therefore excluded from our sample. The collected SNe show a large spread of E_{rad} , with most having a higher value than inferred from the template Type Ibn SNe, and only a few with significantly lower values (SN 2018gix and SN 2020nxt), which may be the effect of a shorter observation campaign or poor multi-band coverage.

The radiated energy from the models scales with the explosion energy $E_{\text{kin,ej}}$ and decreases with very small half-opening angles (cf. Eq. 2-4). The observations with the higher E_{rad} and M_{CSM} align with our models assuming $E_{\text{kin,ej}} = 6 \times 10^{50}$ erg and a spherically distributed-CSM (cf., Fig. 14, bottom-left panel), although, they can still be explained assuming a lower $E_{\text{kin,ej}}$ or a CBD-like CSM with $\theta \geq 15^\circ$. Dimmer events are consistent with significantly lower explosion energies ($E_{\text{kin,ej}} \sim 10^{50}$ erg), expected in the models with the stronger mass-loss and hence smaller final core masses (Sect. 4.3), as well as a thinner CBD-like CSM, with $\theta \lesssim 5^\circ$.

The progenitor and CSM properties inferred from the observed Type Ibn SN we collected can be explained by CBD-like CSM surrounding the binary models explored in this work. However, challenges remain regarding narrow-lines observations. As the narrow lines would originate within the disk, which is likely engulfed by the freely-expanding ejecta in the other directions, the narrow-line component would likely be thermalized and therefore unobservable ([Smith 2017](#)).

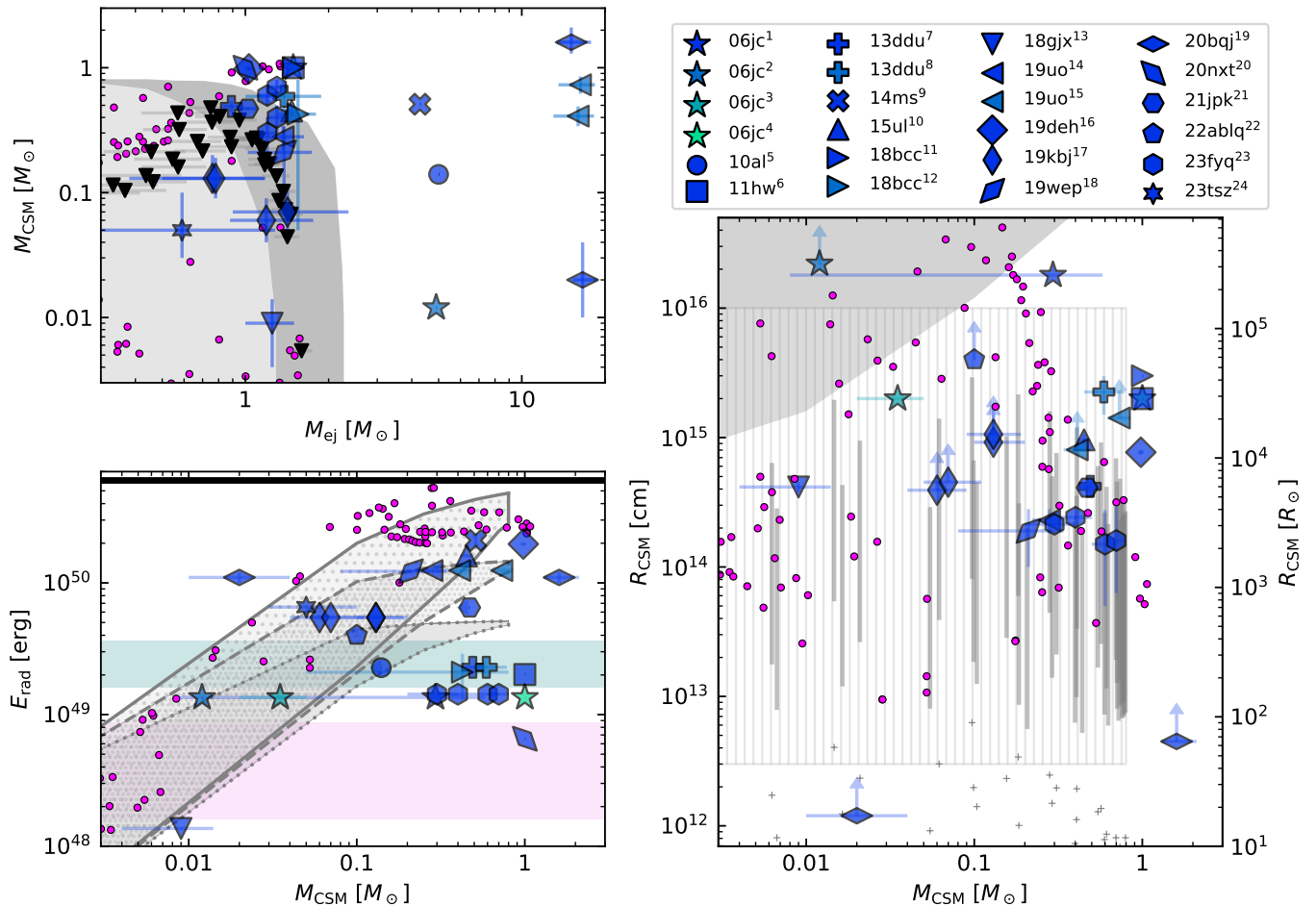


Fig. 14. Comparison between model data and parameters inferred from observed Type Ibn SNe (blue-scale colored markers), with different markers associated to different SNe, and different colors for the same SN highlighting different references. Estimates inferred from the models of WF22 are also included (violet dots). Top Left: Scatter plot showing the amount of mass of the CSM against the ejecta mass in the models as in Fig. 11. As the values of M_{CSM} from the models is an upper limit, a light-gray region is added where models can still be expected. Right: Scatter plot showing the extent of the CSM against its mass. The position of CBD-like CSM from our models is shown with a gray line for $M_{\text{CSM}} = \Delta M_{\text{RLOF-BC}}$. The extrapolated region where to expect CBD from the BG set is shown with a vertically-hatched region. The radii of our theoretical model are also shown (cross scatter). A gray patch is drawn where to expect the CSM if it were to move constantly at a speed of 10 km s^{-1} . Bottom Left: Scatter plot showing the energy released by interaction (Eq. (2)) as a function of CSM mass for the models in this work and WF22 assuming $E_{\text{kin,ej}} = 6 \times 10^{50} \text{ erg}$ (shown with a black horizontal line), and the total light-curve energy of the observed SNe. The shaded regions represent the typical E_{rad} of Type Ibc (light-red, Nicholl et al. 2015) and Type Ibn SNe (light-blue, Hosseinzadeh et al. 2017). The values expected from our models and the BG set are summarized in gray regions, which also show the expected E_{rad} if M_{CSM} is lower than the values inferred. Each gray region assumes that the CSM is distributed spherically (solid line, light-hatch), along a CBD with $\theta = 15^\circ$ (dashed line, dense hatch) and 5° (dotted line, gray fill) of the orbital plane (cf. Eq. (4)).

References: SN2006jc: (1) Mattila et al. 2008; Pastorello et al. 2007 (2) Tominaga et al. 2008; Pastorello et al. 2007 (3) Chugai 2009; Pastorello et al. 2007; (4) Dessart et al. 2022; Pastorello et al. 2007 SN2010al: (5) Chugai 2022; SN2011hw: (6) Dessart et al. 2022; Pastorello et al. 2015b; LSQ13ddu: (7) Pellegrino et al. 2022b; Clark et al. 2020 (8) Clark et al. 2020; Brethauer et al. 2022; ASASSN-15ms: (9) Vallely et al. 2018; iPTF15ul: (10) Pellegrino et al. 2022b; Hosseinzadeh et al. 2017; SN2018bcc: (11) Dessart et al. 2022; Karamehmetoglu et al. 2021; (12) Karamehmetoglu et al. 2021; SN2018gix: (13) Prentice et al. 2020; SN2019uo: (14) Pellegrino et al. 2022b; Gangopadhyay et al. 2020 (15) Gangopadhyay et al. 2020; SN2019deh: (16) Pellegrino et al. 2022b; SN2019kbj: (17) Ben-Ami et al. 2023; SN2019wep: (18) Pellegrino et al. 2022b; Gangopadhyay et al. 2022; SN2020bjj: (19) Kool et al. 2021; SN2020nxt: (20) Wang et al. 2024; SN2021jpk: (21) Pellegrino et al. 2022b; SN2022ablq: (22) Pellegrino et al. 2024; SN2023fyq: (23) Dong et al. 2024; SN2023tsz: (24) Warwick et al. 2024

6.2. Type Icn and Ic-CSM SNe

The observed Type Icn/Ic-CSM SNe feature a diverse sample of events, from the very stripped SN 2023emq ($M_{\text{ej}} \sim 0.3 M_{\odot}$) to the massive Wolf-Rayet progenitor of SN 2010mb ($M_{\text{ej}} > 10 M_{\odot}$). Interestingly, the sample shows a possible correlation between M_{ej} and M_{CSM} , with $M_{\text{ej}} \sim 4 M_{\text{CSM}}$ (cf., Fig. 15, upper-left panel), though this be a result of the low number of observed events. SNe with $M_{\text{ej}} \lesssim 1.5 M_{\odot}$ align with our models

if $M_{\text{CSM}} = \Delta M_{\text{RLOF-BC}}^{(4)}$ (and also $\Delta M_{\text{RLOF-BC}}$ for those that also have $M_{\text{ej}} \geq 1 M_{\odot}$). The ones with higher ejecta and CSM masses (i.e., SN 2010mb, SN 2021ckj, and SN 2022ann) cannot be explained by our models.

The CSM radii in Type Icn SNe are more uncertain than Type Ibn SNe. For example the CSM is inferred to extend from close to the progenitor ($\sim 1 R_{\odot}$, SN 2021csp Pellegrino et al. 2022a) to 10^{15} cm (SN 2019hgp). For some of these SNe, the adoption of different assumptions in the light-curve modeling

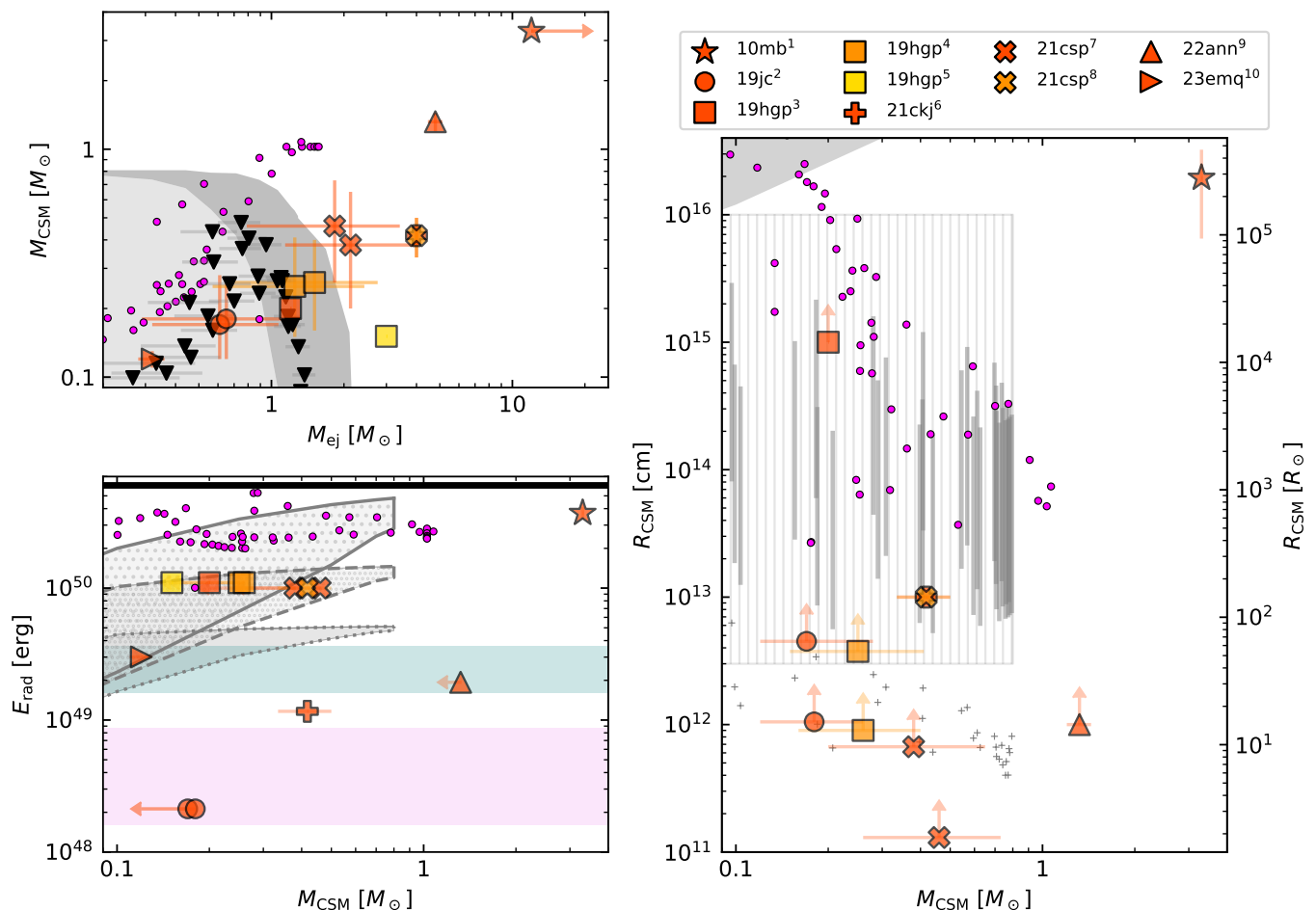


Fig. 15. The same as Fig. 14 but for Type Ic SNe and the Type Ic-CSM SN 2010mb.

References:; SN2010mb: (1) Ben-Ami et al. 2014; Brethauer et al. 2022; SN2019jc: (2) Pellegrino et al. 2022a; SN2019hgp: (3) Gal-Yam et al. 2022 (4) Pellegrino et al. 2022a; Gal-Yam et al. 2022 (5) Nagao et al. 2023; Gal-Yam et al. 2022; SN2021ckj: (6) Nagao et al. 2023; SN2021csp: (7) Pellegrino et al. 2022a; Perley et al. 2022 (8) Nagao et al. 2023; Perley et al. 2022; SN2022ann: (9) Davis et al. 2023; SN2023emq: (10) Pursiainen et al. 2023

changes the value of R_{CSM} by about one order of magnitude (e.g., SN 2019jc, SN 2019hgp and SN 2021csp; cf. Fig. 15, right panel), while M_{ej} and M_{CSM} are not affected by more than a factor of two. The inferred CSM extension in these SNe is compatible with either an extended envelope or a CBD. The slow-moving CSM model can, instead, be ruled out.

The radiated energy of these SNe varies significantly. Brighter events, (e.g., SN 2019hgp, SN 2021csp), align with our models assuming a spherically-symmetric CSM, as well as a CBD-like structure with $\theta > 20^\circ$. Underluminous events (SN 2021ckj and SN 2019jc) are also consistent with our models when considering lower $E_{\text{kin,ej}}$ and a CBD-like CSM with small opening angles.

Similar to the collected Type Ibn SNe, some Type Ic SNe are compatible with the binary channel proposed and a CBD-like CSM structure proposed in this work. However, explaining their spectral evolution remains challenging, especially as the CSM of all our models is He-rich. While there are models with very low He in the ejecta ($\lesssim 0.2 M_{\odot}$, cf. Fig. 10), the metal-rich lines would likely appear broad rather than narrow.

Summary

Our models indicate that Case BC RLOF can produce progenitors and CSM structures broadly consistent with those inferred for a subset of the observed Type Ibn, especially when considering a CSM distributed along a CBD. While our models struggle to fully account for Type Ic/Ic-CSM SNe, the similarities in bulk properties (especially M_{CSM} , M_{ej} and R_{CSM}) and light-curves (cf. Sect. 5.5) warrant further investigation of the spectral evolution in progenitors like those presented in this work.

Caution is warranted when interpreting these results. The CSM mass predicted by our models represents an upper limit, while observational estimates are biased toward a spherically symmetric distribution, which our models disfavor. These discrepancies highlight the need for further investigation of the CSM structure and the interaction features it produces, particularly in the case of a CBD-like configuration.

6.3. Comparisons with Case X RLOF

If the progenitor underwent Case X RLOF, the SN would occur while the system is embedded in a H-poor, He- and metal-rich CE (cf. Sect. 4.1.3 and 4.2.3), which would likely form the CSM. The CE's impact on the light curve would be significant

(as $f_M \sim 1$), likely turning the SN into a SLSN. The CSM structure will be qualitatively different from that generated during Case BC RLOF, due to its more dynamic nature and the shorter timescale before CC.

Case X RLOF has been investigated systematically in WF22 (where the HeS has a NS companion), and they predict M_{CSM} of up to $1 M_\odot$ (cf. Fig. 11). This is still comparable to, or slightly larger than, the mass removed in our models during Case X RLOF (and even Case BC RLOF). However, the timescales and mass transfer rates for Case X RLOF differ significantly: in WF22, Case X RLOF begins even decades before CC, whereas in our models it is confined to only a few weeks or months. In their work, M_{ej} and M_{CSM} are loosely correlated, since their progenitors, which were stripped more (less) during Case BC RLOF, can lose less (more) of their envelope through Case X RLOF before the compact CO-core is completely exposed.

Their constantly expanding CSM (assuming $v_{\text{CSM}} = 200 \text{ km s}^{-1}$) is comparable in size to that of a CBD-like CSM from Case BC RLOF in our models (cf. Figs. 14–15). Since this phase of RLOF is likely unstable and occurs so late in the evolution, the CSM geometry may be more complicated than that of expected from the CSM formed by Case BC RLOF.

The numerical settings used in WF22 are similar to our own, suggesting that their models may also be affected by numerical issues that give rise to this phase of RLOF (see Appendix D for a discussion).

7. Discussion

The results from the models show a series of features that are highly dependent on the assumptions made. We will discuss the main uncertainties affecting our result and provide comparisons to previous works.

7.1. Winds and metallicity

The evolution of the models discussed is strongly influenced by the adopted wind scheme. For HeS mass-loss rates, our models use the prescription from Yoon (2017) (cf. Jin et al. 2024), which combines empirical rates of observed Wolf-Rayet stars with higher luminosities than those found in our models ($\log L/L_\odot > 4.90$ from Nugis & Lamers 2000; Hamann et al. 2006; Hainich et al. 2014; Tramper et al. 2016, against the maximum luminosity before Case BC RLOF in our models of $\log L/L_\odot = 4.75$). This raises the question about the validity of our choice of wind recipes.

Recent studies like Vink (2017) argue for lower mass-loss rates for low-mass HeSs. Gilkis et al. (2019) show that this wind mass-loss rate actually prevents the complete loss of the H-rich envelope if adopted when X_s drops below 0.4. This contrasts with the higher rates predicted by Nugis & Lamers 2000, which our models adopt. Additionally, Göteborg et al. (2023) suggest that the winds of some observed HeSs observed in the LMC and SMC (Drout et al. 2023) are comparable to, or even lower than, those described in Vink (2017).

Significantly weaker winds following Case B RLOF, as would occur with lower initial metallicity, shift the parameter space for Case BC RLOF towards systems with lower initial masses (cf. Sect. 3), because the core remains more massive. A key consequence of weaker winds is that the H-rich envelope may not be completely removed by core He-depletion. This thin H-rich envelope which may be extended enough to also increase the probability of Case BC RLOF (Yoon et al. 2017). If RLOF

does not strip the entire H-rich envelope, the resulting SN will appear as a Type IIb SN with narrow H-lines.

Binary models at lower metallicities also fail to lose the H-rich envelope completely (Yoon et al. 2017; Laplace et al. 2020), due to the reduced winds. In some cases, RLOF may occur before core He-exhaustion (Klencki et al. 2022), which can be followed again by Case BC RLOF to further strip down the envelope.

The shift in Case BC parameter space towards lower initial masses does increase the likelihood of observing interacting SNe (which may not necessarily be H-poor). This is due to a combination of lower-mass models developing more massive cores and the IMF favoring the production of lower-mass stars (Salpeter 1955).

7.2. Mass transfer

7.2.1. Mass accretion and angular-momentum loss

The amount of mass accreted by the companion star during mass transfer and the amount of angular momentum carried away by unaccreted material are critical parameters influencing the evolution of mass-transferring binaries (Podsiadlowski et al. 1992). We report the key effects on our models, and we refer to Ercolino et al. (2024) (and references therein) for a more detailed discussion.

Angular momentum losses may exceed those accounted for in our models due to additional mechanisms. For example, outflows from the outer Lagrangian point of the accretor, that may occur when mass transfer rates exceed $10^{-4} M_\odot \text{ yr}^{-1}$ (Lu et al. 2023), can carry away significant angular-momentum. Furthermore, unaccreted material remaining in the vicinity of the system can exchange angular momentum with the inner binary. In the presence of a CBD, additional processes such as mass reaccretion, angular momentum exchanges and eccentricity pumping may also occur (e.g., Wei et al. 2024; Valli et al. 2024). Higher angular momentum losses would tighten the orbit during RLOF and therefore remove more mass from the donor star.

For Case B RLOF, increase angular momentum losses would result in smaller $M_{\text{He-dep}}$ and $R_{\text{RL,1}}$, which would increase the parameter space for Case BC RLOF. However, this would also make mass transfer more prone to becoming unstable (Willcox et al. 2023). In the context of Case BC RLOF, these effects will likely lead to more mass-loss and therefore larger M_{CSM} . In this case however, the stability of mass transfer would likely remain unaffected due to the significantly more massive companion and contained mass-loss.

Our models may also underestimate the amount of mass accreted by the secondary (Vinciguerra et al. 2020). Increase in mass transfer efficiency would remove more mass from the donor (e.g. Claeys et al. 2011), expanding the parameter space for Case BC RLOF to occur as well as increasing the likelihood of mass transfer turning unstable (Braun & Langer 1995; Schürmann & Langer 2024). Increased accretion efficiency would reduce the amount of CSM as more of the transferred mass would be deposited on the companion star, rather than lost from the system.

7.2.2. Stability of Mass transfer

Even though the computation of mass transfer proceeds unimpeded, special care is required to ensure the results have physical significance. This includes verifying whether the underlying assumptions hold during the calculations (Temmink et al. 2023)

or determining if the system enters an unstable phase of mass transfer. The criteria for identifying unstable mass transfer remain debated and we discuss a few in the context of Case B and Case BC RLOF below. We will not discuss the effects on Case X RLOF here (but see Sect. 4.2.3).

Our calculations assume that unaccreted material is ejected as a fast wind from the secondary star (Soberman et al. 1997). However, there is a limited understanding of how the unaccreted material escapes the inner binary. If it is not ejected efficiently, it may exert drag and extract orbital angular momentum, driving the system into an unstable phase of RLOF.

Marchant (2017) proposes that the unaccreted material can be ejected via a radiation-driven wind, which defines an upper limit on the mass transfer rate \dot{M}_{high} . This rate represents the threshold above which the combined luminosity of the two stars is not able to drive the material away radiatively. The un-accreted material is assumed to lie on the outer edges of the accretion disk, at a distance $R_{\text{RL},2}$ from the secondary star, and the limit is given by

$$\dot{M}_{\text{high}} = (L_1 + L_2) \frac{R_{\text{RL},2}^2}{GM_2}, \quad (5)$$

where M_2 is the mass of the secondary, and L_1 and L_2 the luminosities of the primary and secondary stars respectively. If mass transfer is inefficient and $\dot{M}_{\text{RLOF}} > \dot{M}_{\text{high}}$, the system cannot remove the unaccreted material from the inner binary, leading to unstable RLOF. Fig. 16 illustrates a slice of the parameter space of Case BC systems at $M_{1,i} = 12.6 M_{\odot}$, revealing that many systems but those with high P_i or q_i would undergo CE evolution during Case B RLOF. This is because during Case B RLOF the donor star temporarily dims as it is thrown off of thermal equilibrium. Unless the binary is wide or the companion is very luminous, this instability criterion is met. In our models, where $q_i = 0.5$, are always flagged as unstable according to this criterion.

Pauli (2020) argues that during the short timescale in which the primary star dims, the material can still be pushed away from the inner binary to a finite distance from the system before the primary resettles to a higher luminosity. This may subsequently enable the radiation-driven ejection of the material. They argue that in Eq. (5), L_1 should be replaced by the maximum luminosity reached by the donor during mass transfer. This makes the criterion less stringent than that of Marchant (2017), classifying only the models with the lowest q_i and P_i as unstable during Case B RLOF. In our rerun models, this affects only the models with $P_i < 10$ d.

Figure 16 highlights the systems expected to undergo Case BC RLOF. Using the stricter criterion from Marchant (2017) significantly reduces the parameter space for the binaries that survive Case B RLOF. For instance, in the grid at $M_{1,i} = 12.6 M_{\odot}$, most models predicted to experience Case BC RLOF (which give rise to H-poor interacting SNe) would instead have undergone unstable Case B RLOF and likely merge (likely producing a Type II SN progenitor). By contrast, the criterion from Pauli et al. (2022) only excludes a handful of systems. Both criteria flag more systems as stable with increasing $M_{1,i}$ due to the higher luminosities.

Another indicator of the onset of unstable RLOF is when the donor star swells to the point of undergoing OLOF (Pavlovskii & Ivanova 2015; Ercolino et al. 2024). In this case, the results in the BG set differ from the binaries we rerun. Due to the inclusion of radiation pressure in the mass-transfer scheme (cf. Sect. 2.4), the donor stars in our models do not expand as much as in the

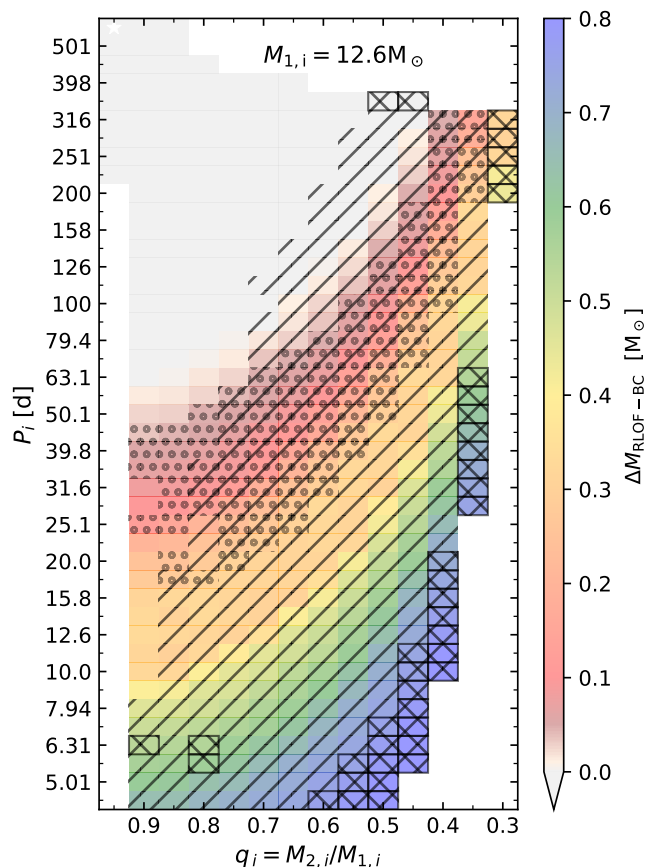


Fig. 16. The $\log P_i - q_i$ diagram of the the Case B binary models in the BG set with $M_{1,i} = 12.6 M_{\odot}$, color-coded based on the amount of mass expected to be shed during Case BC RLOF. The hatching indicates models that are flagged as having undergone unstable Case B RLOF according to the criterion from Marchant (2017) (single hatch), Pauli (2020) (cross hatch) and Pavlovskii & Ivanova (2015) (circle hatches).

BG set during Case B mass transfer, and therefore do not exhibit OLOF, even in cases where OLOF is flagged in the BG models. Case BC RLOF is never flagged as unstable per the criterion from Pavlovskii & Ivanova (2015).

Our analysis demonstrates that applying different mass transfer stability criteria to the same 1D simulations significantly alters the predicted outcome, particularly for the first phase of mass transfer (i.e., Case B RLOF in these systems, and a similar discussion also holds for those undergoing Case A RLOF). Conversely, Case BC RLOF is consistently stable across all the criteria mentioned, as the mass-loss rates are much lower, the donor does not expand significantly, and the mass ratio is inverted.

7.3. Uncertainties in the latter evolutionary stages: the case for eruptions before CC

Precursors to the SN explosion have been observed for some interacting SNe (e.g., Strotjohann et al. 2021). Among Type Ibn SNe, pre-explosion outbursts have been observed for SN 2006jc (Pastorello et al. 2007), SN 2019uo (Strotjohann et al. 2021), and SN 2023fyq (Brennan et al. 2024; Dong et al. 2024). It is not yet clear if these outbursts are characteristic of all Type Ibn progenitors. In some cases, pre-explosion photometry rules out the presence of bright precursors, like SN 2015G (Shivvers et al.

2017), SN 2020nxt (Wang et al. 2024), and SN 2022ablq (Pellegrino et al. 2024).

These outbursts may drive intense mass-loss, providing an alternative mechanism to produce the nearby CSM observed in many Type Ibn SNe (Dessart et al. 2022; Maeda & Moriya 2022; Takei et al. 2024). Simulations of SNe with progenitors similar to those in this work were carried out by (Dessart et al. 2022), where they included a CSM formed by an eruption in the last $\lesssim 2$ yr before CC. They find that an outburst-driven CSM leads to light-curve and spectral features compatible to observations of Type Ibn events.

Lower-mass models can experience Si-flashes (Woosley & Heger 2015; Woosley 2019) that release sufficient energy to expand, or even unbind, parts of the envelope. This expansion may also be triggered by Ne-flashes (Wu & Fuller 2022b). In Woosley & Heger (2015), these flashes impact models with $M_{\text{CO,end}} < 1.68 M_{\odot}$, which correspond to about half of the models investigated here. While our models lack the proper physics to account for this effect, we argue that the sudden expansion alone can trigger Case X RLOF and create a close-by and dense CSM, perhaps even accompanied by an observable pre-SN outburst.

7.4. CSM geometry surrounding a binary

The structure of the CSM in our models depends on the mechanism that drives the ejection of unaccreted material. If the material is lost through isotropic re-emission (Soberman et al. 1997), it would distribute evenly in all directions. Alternatively, if it is lost through the accretor’s outer Lagrangian point, it may accumulate near the orbital plane (e.g. Lu et al. 2023) and form a bound CBD. Such a disk could retain a significant fraction of the unaccreted mass (at least 80% of the mass lost during Case BC RLOF, Pejcha et al. 2016). The presence of such massive CBD will also introduce a complex shock geometry, particularly at the boundary regions of the disk.

The recent work of Tuna & Metzger (2023) offers an analytical description of the CBD’s evolution but for the case of a post-CE CBD. While the evolutionary history of disks in our models differ, their findings offer relevant insight. They suggest that the CBD may persist for ~ 50 kyr, with most of its mass lost through reaccretion onto the inner binary, while only a small fraction is lost by photoevaporation (Hollenbach et al. 1994). In contrast, in our models, the CBD would be continuously supplied with mass by the inner binary. The extension of the CBD – which is determined by the region where photo-evaporation dominates – depends on parameters of the inner binary such as its mass and total luminosity, as well as composition and temperature of the disk (Tuna & Metzger 2023), which we have neglected here.

While we assume that the CSM is entirely contained within a CBD or freely expanding in all directions, the reality is likely more complex. It is reasonable to expect that, while the binary loses material to form a CBD, a fraction of the material can be lost through other mechanisms (e.g., isotropic re-emission, Soberman et al. 1997) resulting in a multicomponent CSM. Thus, while the assumption that the RLOF-induced CSM impacts the SN is reasonable, significant uncertainties remain about its mass, extent, and geometry.

Low-mass HeS with high L/M ratios are expected to be pulsationally unstable (Saio et al. 1984; Gautschy et al. 1990; Gautschy & Saio 1995). This is due to the expansion following core He depletion where the outer regions of the envelope experience HeII recombination and become locally super-Eddington, producing a density inversion. These pulsations could trigger

episodic phases of mass transfer, as the star would periodically fill the Roche Lobe, therefore losing more mass and further increasing its L/M . These pulsations could therefore produce a more mass loaded CSM, similar to what is expected in the case of a wide RSG+MS mass-transferring binary (Ercolino et al. 2024).

7.5. Comparison to previous works

The mass transfer phase we focused on in our models (Case BC RLOF) results from the expansion of low-mass HeS, a phenomenon well-documented in the literature (Paczynski 1971; Habets 1986; Tauris et al. 2013, 2015; Kleiser et al. 2018; Woosley 2019; Laplace et al. 2020), which our models replicate qualitatively well. Many previous studies of HeSs undergoing RLOF focused on systems with a compact object companion (NS or BH) following a phase of CE-evolution (e.g., Dewi & Pols 2003; Tauris et al. 2013, 2015; Jiang et al. 2021, 2023, WF22, Wei et al. 2024; Guo et al. 2024; Qin et al. 2024). In such HeS+NS binaries, the mass ratio during Case BC RLOF is typically < 0.5 , which is significantly lower than our systems. As a result, their orbit shrinks during RLOF, whereas ours expands, leading to more mass being transferred overall (see also Appendix B). For the HeS+NS systems mentioned above, typical orbital periods are in the order of a few days or less, which can allow the HeSs to fill their Roche lobes during or immediately after core He burning, allowing for more overall stripping than in our models. Such a tight binary with instead a MS companion do not emerge in the BG grid (Sect. 3.2).

One work that modeled RLOF between a HeS and a MS companion was Habets (1986). In their work, RLOF occurs in a very tight orbit ($M_{\text{HeS}} = 2.5 M_{\odot}$, $R_{\text{RL},1} = 1 R_{\odot}$, $M_2 = 17 M_{\odot}$), removing about $0.3 M_{\odot}$ of the HeS’s envelope. This is much less than what we expect from our models, which may be attributable to differences in physical assumptions.

One of our main concerns from our method was the adoption of a limited nuclear network (cf. Sect. 2.2), especially during the final evolutionary phases. Prior studies in the literature that have adopted larger nuclear networks during Case BC RLOF show results broadly consistent to ours (e.g., Jiang et al. 2021, 2023), with some even showcasing Case X RLOF (Wei et al. 2024; Guo et al. 2024). In Jiang et al. (2021, 2023), where they studied HeS+NS/BH binaries with an detailed nuclear network, mass transfer rates in the last months prior to collapse (i.e., Case X RLOF) were noted to be sensitive to some solver flags (their models, however, do not reach rates comparable to the extreme ones of our models). They were able to derive the SN-explosion properties from their least massive model, which yielded an explosion energy of 6×10^{50} erg and a remnant mass of $1.34 M_{\odot}$. These values are compatible with the ones adopted in this paper (cf. Sect. 4.3).

8. Conclusions

In this work, we investigated a comprehensive set of binary evolution models. We focus on those in which the primary is stripped to become a helium star after core hydrogen depletion, and undergoes a second mass transfer phase with a main-sequence companion after core helium exhaustion up until close to core-collapse. The later phase of mass transfer is triggered in the systems where the helium-star primary has a mass of less than $3.4 M_{\odot}$ by the time of core He-depletion. During this phase, the amount of mass lost depends on how early mass transfer begins, which can remove as much as $0.8 M_{\odot}$ of the He-rich

envelope for the models that started about 20 kyr before core-collapse.

In our binary models, the main-sequence companion does not accrete significant amounts of the transferred material, which instead is lost from the system to form a nearby, H-free, circumbinary medium. Its typical mass of $0.4 M_{\odot}$ is large enough to give rise to significant interaction features, especially by extracting kinetic energy from the impacting supernova ejecta, which can be as high as 70%. Using a simplified model that neglects diffusion, we explore the impacts of different structures of the circumbinary material on the supernova light-curve. A circumbinary disk-like structure qualitatively reproduces the light-curve morphology of many Type Ibn supernovae.

We find that our models produce masses and radii of the circumbinary material, as well as ejecta masses and integrated bolometric luminosities, which are compatible with those observed in many Type Ibn supernovae. However, these studies mostly assume a spherical distribution of the material, while our results show that a disk-like distribution is another reasonable possibility. Future studies on the evolution of the circumbinary material produced by binary mass-transfer will be crucial to address the structure and geometry of the material at core-collapse. This simultaneously calls for future research to explore how these large-scale asymmetries influence the light-curve and spectral evolution of interacting supernovae, and how these factors impact inferred properties from the observed data.

Finally, we developed a method to map the properties of a binary model at core He-depletion to the amount of mass being transferred during the later phase of mass-transfer. Applying this to a comprehensive grid of binary models, we find that 12% of all stripped-envelope SN progenitors produced in binaries are expected to undergo mass-transfer until core-collapse, and can therefore be expected to become H-poor interacting supernovae, which is in broad agreement with observational rate estimates of Type Ibn SNe (Perley et al. 2020). Future observations from ongoing surveys like ZTF, and the beginning of the science operations of LSST in 2025, will yield more significant constraints on the observed population of these supernovae.

Acknowledgements. AE is grateful for the discussions with Lorenzo Roberti, David R. Aguilera-Dena, Thomas Tauris, Christoph Schürmann, Eva Laplace, Alexander Heger and Ruggero Valli. AE acknowledges the support from the DFG through grant LA 587/22-1.

References

Aguilera-Dena, D. R., Langer, N., Antoniadis, J., et al. 2022, *A&A*, 661, A60
Aguilera-Dena, D. R., Langer, N., Moriya, T. J., & Schootemeijer, A. 2018, *ApJ*, 858, 115
Aguilera-Dena, D. R., Müller, B., Antoniadis, J., et al. 2023, *A&A*, 671, A134
Arnett, W. D. 1982, *ApJ*, 253, 785
Artymowicz, P. & Lubow, S. H. 1994, *ApJ*, 421, 651
Asplund, M., Amarsi, A. M., & Grevesse, N. 2021, *A&A*, 653, A141
Bellm, E. C., Kulkarni, S. R., Graham, M. J., et al. 2019, *PASP*, 131, 018002
Ben-Ami, S., Gal-Yam, A., Mazzali, P. A., et al. 2014, *ApJ*, 785, 37
Ben-Ami, T., Arcavi, I., Newsome, M., et al. 2023, *ApJ*, 946, 30
Braun, H. & Langer, N. 1995, *A&A*, 297, 483
Brennan, S. J., Sollerman, J., Irani, I., et al. 2024, *A&A*, 684, L18
Brethauer, D., Margutti, R., Milisavljevic, D., et al. 2022, *ApJ*, 939, 105
Burrows, A., Hayes, J., & Fryxell, B. A. 1995, *ApJ*, 450, 830
Chatzopoulos, E., Wheeler, J. C., & Vinko, J. 2012, *ApJ*, 746, 121
Chatzopoulos, E., Wheeler, J. C., Vinko, J., Horvath, Z. L., & Nagy, A. 2013, *ApJ*, 773, 76
Chen, P., Gal-Yam, A., Sollerman, J., et al. 2024, *Nature*, 625, 253
Chen, Z. H., Yan, L., Kangas, T., et al. 2023, *ApJ*, 943, 42
Chugai, N. N. 2009, *MNRAS*, 400, 866
Chugai, N. N. 2022, *Astronomy Letters*, 48, 163
Chugai, N. N., Blinnikov, S. I., Cumming, R. J., et al. 2004, *MNRAS*, 352, 1213

Claeys, J. S. W., de Mink, S. E., Pols, O. R., Eldridge, J. J., & Baes, M. 2011, *A&A*, 528, A131
Clark, P., Maguire, K., Inseerra, C., et al. 2020, *MNRAS*, 492, 2208
Darwin, G. H. 1879, *Proceedings of the Royal Society of London Series I*, 29, 168
Das, K. K., Fremling, C., Kasliwal, M. M., et al. 2024a, *ApJ*, 969, L11
Das, K. K., Kasliwal, M. M., Sollerman, J., et al. 2024b, *ApJ*, 972, 91
Davis, K. W., Taggart, K., Tinianont, S., et al. 2023, *MNRAS*, 523, 2530
De, K., Kasliwal, M. M., Cantwell, T., et al. 2018a, *ApJ*, 866, 72
De, K., Kasliwal, M. M., Ofek, E. O., et al. 2018b, *Science*, 362, 201
De, K., Kasliwal, M. M., Tzanidakis, A., et al. 2020, *ApJ*, 905, 58
Dessart, L., Gutiérrez, C. P., Ercolino, A., Jin, H., & Langer, N. 2024, *A&A*, 685, A169
Dessart, L. & Hillier, D. J. 2022, *A&A*, 660, L9
Dessart, L., Hillier, D. J., & Kuncarayakti, H. 2022, *A&A*, 658, A130
Dessart, L., Hillier, D. J., Li, C., & Woosley, S. 2012, *MNRAS*, 424, 2139
Dessart, L., Hillier, D. J., Livne, E., et al. 2011, *MNRAS*, 414, 2985
Dessart, L., Hillier, D. J., Sukhbold, T., Woosley, S. E., & Janka, H. T. 2021, *A&A*, 656, A61
Dessart, L., Hillier, D. J., Woosley, S. E., & Kuncarayakti, H. 2023, *A&A*, 677, A7
Dessart, L., Yoon, S.-C., Aguilera-Dena, D. R., & Langer, N. 2020, *A&A*, 642, A106
Dewi, J. D. M. & Pols, O. R. 2003, *MNRAS*, 344, 629
Dong, Y., Tsuna, D., Valenti, S., et al. 2024, arXiv e-prints, arXiv:2405.04583
Drout, M. R., Götzberg, Y., Ludwig, B. A., et al. 2023, *Science*, 382, 1287
Dufton, P. L., Langer, N., Dunstall, P. R., et al. 2013, *A&A*, 550, A109
Ercolino, A., Jin, H., Langer, N., & Dessart, L. 2024, *A&A*, 685, A58
Ertini, K., Folatelli, G., Martinez, L., et al. 2023, *MNRAS*, 526, 279
Ertl, T., Woosley, S. E., Sukhbold, T., & Janka, H. T. 2020, *ApJ*, 890, 51
Farmer, R., Fields, C. E., Petermann, I., et al. 2016, *ApJS*, 227, 22
Gal-Yam, A., Bruch, R., Schulze, S., et al. 2022, *Nature*, 601, 201
Gangopadhyay, A., Misra, K., Hiramatsu, D., et al. 2020, *ApJ*, 889, 170
Gangopadhyay, A., Misra, K., Hosseinzadeh, G., et al. 2022, *ApJ*, 930, 127
Gautschi, A., Glatzel, W., Gautschi, A., & Glatzel, W. 1990, *MNRAS*, 245, 597
Gautschi, A. & Saio, H. 1995, *ARA&A*, 33, 75
Gilks, A., Vink, J. S., Eldridge, J. J., & Tout, C. A. 2019, *MNRAS*, 486, 4451
Gomez, S., Nicholl, M., Berger, E., et al. 2024, *MNRAS*, 535, 471
Götzberg, Y., Drout, M. R., Ji, A. P., et al. 2023, *ApJ*, 959, 125
Guillochon, J., Nicholl, M., Villar, V. A., et al. 2018, *ApJS*, 236, 6
Guo, Y.-L., Wang, B., Chen, W.-C., et al. 2024, *MNRAS*, 530, 4461
Habets, G. M. H. J. 1986, *A&A*, 165, 95
Hainich, R., Rühling, U., Todt, H., et al. 2014, *A&A*, 565, A27
Hamann, W. R., Gräfener, G., & Liermann, A. 2006, *A&A*, 457, 1015
Hastings, B., Langer, N., Wang, C., Schootemeijer, A., & Milone, A. P. 2021, *A&A*, 653, A144
Heger, A., Langer, N., & Woosley, S. E. 2000, *ApJ*, 528, 368
Heger, A., Woosley, S. E., & Spruit, H. C. 2005, *ApJ*, 626, 350
Hirai, R. 2023, *MNRAS*, 523, 6011
Hirai, R., Podsiadlowski, P., & Yamada, S. 2018, *ApJ*, 864, 119
Ho, A. Y. Q., Perley, D. A., Gal-Yam, A., et al. 2023, *ApJ*, 949, 120
Hollenbach, D., Johnstone, D., Lizano, S., & Shu, F. 1994, *ApJ*, 428, 654
Hosseinzadeh, G., Arcavi, I., Valenti, S., et al. 2017, *ApJ*, 836, 158
Ivezić, Ž., Kahn, S. M., Tyson, J. A., et al. 2019, *ApJ*, 873, 111
Jacobson-Galán, W. V., Margutti, R., Kilpatrick, C. D., et al. 2020, *ApJ*, 898, 166
Jacobson-Galán, W. V., Venkatraman, P., Margutti, R., et al. 2022, *ApJ*, 932, 58
Janka, H.-T. 2017, *ApJ*, 837, 84
Jiang, L., Chen, W.-C., Tauris, T. M., Müller, B., & Li, X.-D. 2023, *ApJ*, 945, 90
Jiang, L., Tauris, T. M., Chen, W.-C., & Fuller, J. 2021, *ApJ*, 920, L36
Jin, H., Langer, N., Lennon, D. J., & Proffitt, C. R. 2024, *A&A*, 690, A135
Karamahmetoglu, E., Fransson, C., Sollerman, J., et al. 2021, *A&A*, 649, A163
Khatami, D. K. & Kasen, D. N. 2019, *ApJ*, 878, 56
Kleiser, I., Fuller, J., & Kasen, D. 2018, *MNRAS*, 481, L141
Klencki, J., Istrate, A., Nelemans, G., & Pols, O. 2022, *A&A*, 662, A56
Kochanek, C. S., Shappee, B. J., Stanek, K. Z., et al. 2017, *PASP*, 129, 104502
Kolb, U. & Ritter, H. 1990, *A&A*, 236, 385
Kool, E. C., Karamahmetoglu, E., Sollerman, J., et al. 2021, *A&A*, 652, A136
Kruckow, M. U., Tauris, T. M., Langer, N., Kramer, M., & Izzard, R. G. 2018, *MNRAS*, 481, 1908
Kulkarni, S. R. 2013, *The Astronomer's Telegram*, 4807, 1
Laplace, E., Götzberg, Y., de Mink, S. E., Justham, S., & Farmer, R. 2020, *A&A*, 637, A6
Law, N. M., Kulkarni, S. R., Dekany, R. G., et al. 2009, *PASP*, 121, 1395
Liu, Z.-W., Röpke, F. K., & Han, Z. 2023, *Research in Astronomy and Astrophysics*, 23, 082001
Liu, Z.-W., Tauris, T. M., Röpke, F. K., et al. 2015, *A&A*, 584, A11
Lu, W., Fuller, J., Quataert, E., & Bonnerot, C. 2023, *MNRAS*, 519, 1409
Lucy, L. B. 1991, *ApJ*, 383, 308
Maeda, K. & Moriya, T. J. 2022, *ApJ*, 927, 25
Mandel, I. & Müller, B. 2020, *MNRAS*, 499, 3214

- Marchant, P. 2017, PhD thesis, Rheinische Friedrich Wilhelms University of Bonn, Germany
- Marchant, P., Langer, N., Podsiadlowski, P., Tauris, T. M., & Moriya, T. J. 2016, *A&A*, 588, A50
- Marchant, P., Pappas, K. M. W., Gallegos-Garcia, M., et al. 2021, *A&A*, 650, A107
- Margutti, R., Metzger, B. D., Chornock, R., et al. 2019, *ApJ*, 872, 18
- Matsuoka, T. & Sawada, R. 2024, *ApJ*, 963, 105
- Mattila, S., Meikle, W. P. S., Lundqvist, P., et al. 2008, *MNRAS*, 389, 141
- Metzger, B. D., Margalit, B., Kasen, D., & Quataert, E. 2015, *MNRAS*, 454, 3311
- Moore, T., Gillanders, J., Nicholl, M., et al. 2024, arXiv e-prints, arXiv:2405.13596
- Moore, T., Smartt, S. J., Nicholl, M., et al. 2023, *ApJ*, 956, L31
- Müller, B., Heger, A., Liptai, D., & Cameron, J. B. 2016, *MNRAS*, 460, 742
- Nagao, T., Kuncarayakti, H., Maeda, K., et al. 2023, *A&A*, 673, A27
- Nakaoka, T., Maeda, K., Yamanaka, M., et al. 2021, *ApJ*, 912, 30
- Nicholl, M., Smartt, S. J., Jerkstrand, A., et al. 2015, *MNRAS*, 452, 3869
- Nugis, T. & Lamers, H. J. G. L. M. 2000, *A&A*, 360, 227
- O'Connor, E. & Ott, C. D. 2011, *ApJ*, 730, 70
- Ogata, M., Hirai, R., & Hijikawa, K. 2021, *MNRAS*, 505, 2485
- Ouchi, R. & Maeda, K. 2017, *ApJ*, 840, 90
- Paczyński, B. 1971, *Acta Astron.*, 21, 1
- Pastorello, A., Benetti, S., Brown, P. J., et al. 2015a, *MNRAS*, 449, 1921
- Pastorello, A., Benetti, S., Brown, P. J., et al. 2015b, *MNRAS*, 449, 1921
- Pastorello, A., Smartt, S. J., Mattila, S., et al. 2007, *Nature*, 447, 829
- Pauli, D. 2020, Master's thesis, Rheinische Friedrich Wilhelms University of Bonn, Germany
- Pauli, D., Langer, N., Aguilera-Dena, D. R., Wang, C., & Marchant, P. 2022, *A&A*, 667, A58
- Pavlovskii, K. & Ivanova, N. 2015, *MNRAS*, 449, 4415
- Paxton, B., Bildsten, L., Dotter, A., et al. 2011, *ApJS*, 192, 3
- Paxton, B., Cantiello, M., Arras, P., et al. 2013, *ApJS*, 208, 4
- Paxton, B., Marchant, P., Schwab, J., et al. 2015, *ApJS*, 220, 15
- Paxton, B., Schwab, J., Bauer, E. B., et al. 2018, *ApJS*, 234, 34
- Paxton, B., Smolec, R., Schwab, J., et al. 2019, *ApJS*, 243, 10
- Pejcha, O., Metzger, B. D., & Tomida, K. 2016, *MNRAS*, 455, 4351
- Pellegrino, C., Howell, D. A., Terreran, G., et al. 2022a, *ApJ*, 938, 73
- Pellegrino, C., Howell, D. A., Vinkó, J., et al. 2022b, *ApJ*, 926, 125
- Pellegrino, C., Modjaz, M., Takei, Y., et al. 2024, arXiv e-prints, arXiv:2407.18291
- Perley, D. A., Fremling, C., Sollerman, J., et al. 2020, *ApJ*, 904, 35
- Perley, D. A., Sollerman, J., Schulze, S., et al. 2022, *ApJ*, 927, 180
- Petrovic, J., Langer, N., & van der Hucht, K. A. 2005, *A&A*, 435, 1013
- Podsiadlowski, P., Joss, P. C., & Hsu, J. J. L. 1992, *ApJ*, 391, 246
- Prentice, S. J., Maguire, K., Boian, I., et al. 2020, *MNRAS*, 499, 1450
- Pursiainen, M., Leloudas, G., Schulze, S., et al. 2023, *ApJ*, 959, L10
- Qin, Y., Zhu, J.-P., Meynet, G., et al. 2024, arXiv e-prints, arXiv:2409.10869
- Quataert, E. & Shiode, J. 2012, *MNRAS*, 423, L92
- Richards, S., Eldridge, J., Ghodla, S., & Briel, M. 2024, arXiv e-prints, arXiv:2411.03000
- Saio, H., Wheeler, J. C., & Cox, J. P. 1984, *ApJ*, 281, 318
- Salpeter, E. E. 1955, *ApJ*, 121, 161
- Sana, H., de Mink, S. E., de Koter, A., et al. 2012, *Science*, 337, 444
- Schulze, S., Gal-Yam, A., Dessart, L., et al. 2024, arXiv e-prints, arXiv:2409.02054
- Schürmann, C. & Langer, N. 2024, *A&A*, 691, A174
- Shivkumar, H., Jaodand, A. D., Balasubramanian, A., et al. 2023, *ApJ*, 952, 86
- Shivvers, I., Zheng, W., Van Dyk, S. D., et al. 2017, *MNRAS*, 471, 4381
- Smith, N. 2017, in *Handbook of Supernovae*, ed. A. W. Alsabti & P. Murdin, 403
- Smith, N. & Arnett, W. D. 2014, *ApJ*, 785, 82
- Smith, N., Kilpatrick, C. D., Mauerhan, J. C., et al. 2017, *MNRAS*, 466, 3021
- Soberman, G. E., Phinney, E. S., & van den Heuvel, E. P. J. 1997, *A&A*, 327, 620
- Sravan, N., Marchant, P., & Kalogera, V. 2019, *ApJ*, 885, 130
- Strotjohann, N. L., Ofek, E. O., Gal-Yam, A., et al. 2021, *ApJ*, 907, 99
- Sukhbold, T. & Woosley, S. E. 2014, *ApJ*, 783, 10
- Suzuki, A., Moriya, T. J., & Takiwaki, T. 2019, *ApJ*, 887, 249
- Takei, Y., Tsuna, D., Ko, T., & Shigejima, T. 2024, *ApJ*, 961, 67
- Tauris, T. M., Langer, N., Moriya, T. J., et al. 2013, *ApJ*, 778, L23
- Tauris, T. M., Langer, N., & Podsiadlowski, P. 2015, *MNRAS*, 451, 2123
- Temmink, K. D., Pols, O. R., Justham, S., Istrate, A. G., & Toonen, S. 2023, *A&A*, 669, A45
- Tominaga, N., Limongi, M., Suzuki, T., et al. 2008, *ApJ*, 687, 1208
- Tonry, J. L., Denneau, L., Heinze, A. N., et al. 2018, *PASP*, 130, 064505
- Tramper, F., Sana, H., & de Koter, A. 2016, *ApJ*, 833, 133
- Tuna, S. & Metzger, B. D. 2023, *ApJ*, 955, 125
- Turatto, M. & Pastorello, A. 2014, in *Supernova Environmental Impacts*, ed. A. Ray & R. A. McCray, Vol. 296, 63–67
- Vallely, P. J., Prieto, J. L., Stanek, K. Z., et al. 2018, *MNRAS*, 475, 2344
- Valli, R., Tiede, C., Vigna-Gómez, A., et al. 2024, *A&A*, 688, A128
- Villar, V. A., Berger, E., Metzger, B. D., & Guillochon, J. 2017, *ApJ*, 849, 70
- Vinciguerra, S., Neijssel, C. J., Vigna-Gómez, A., et al. 2020, *MNRAS*, 498, 4705
- Vink, J. S. 2017, *A&A*, 607, L8
- Vlasis, A., Dessart, L., & Audit, E. 2016, *MNRAS*, 458, 1253
- Wang, Q., Goel, A., Dessart, L., et al. 2024, *MNRAS*, 530, 3906
- Warwick, B., Lyman, J., Pursiainen, M., et al. 2024, arXiv e-prints, arXiv:2409.14147
- Wei, D., Schneider, F. R. N., Podsiadlowski, P., et al. 2024, *A&A*, 688, A87
- Wellstein, S. & Langer, N. 1999, *A&A*, 350, 148
- Willcox, R., MacLeod, M., Mandel, I., & Hirai, R. 2023, *ApJ*, 958, 138
- Woosley, S. E. 2019, *ApJ*, 878, 49
- Woosley, S. E. & Heger, A. 2015, *ApJ*, 810, 34
- Woosley, S. E., Langer, N., & Weaver, T. A. 1995, *ApJ*, 448, 315
- Woosley, S. E., Sukhbold, T., & Kasen, D. N. 2021, *ApJ*, 913, 145
- Woosley, S. E., Weaver, T. A., & Taam, R. E. 1980, in *Texas Workshop on Type I Supernovae*, ed. J. C. Wheeler, 96–112
- Worley, A., Krastev, P. G., & Li, B.-A. 2008, *ApJ*, 685, 390
- Wu, S. & Fuller, J. 2021, *ApJ*, 906, 3
- Wu, S. C. & Fuller, J. 2022a, *ApJ*, 940, L27
- Wu, S. C. & Fuller, J. 2022b, *ApJ*, 930, 119
- Yadav, N., Müller, B., Janka, H. T., Melson, T., & Heger, A. 2020, *ApJ*, 890, 94
- Yan, S., Wang, X., Gao, X., et al. 2023, *ApJ*, 959, L32
- Yao, Y., De, K., Kasliwal, M. M., et al. 2020, *ApJ*, 900, 46
- Yoon, S.-C. 2017, *MNRAS*, 470, 3970
- Yoon, S.-C., Dessart, L., & Clocchiatti, A. 2017, *ApJ*, 840, 10
- Yoon, S. C., Woosley, S. E., & Langer, N. 2010, *ApJ*, 725, 940

Appendix A: Parameter space from Case A systems

Compared to Case B systems, models undergoing Case A RLOF will develop less massive cores due to the extreme mass loss during the MS which shrinks the convective H-burning core. This means that the parameter space for CC progenitors moves to higher initial masses compared to Case B systems (cf. Fig. 2). Case AB RLOF follows after TAMS, which allows the primaries to be fully stripped soon after core He ignition.

Just like the Case B systems (Sect. 3.2), the orbit following Case AB RLOF is wide enough to again allow RLOF only after core He depletion (cf. Fig. 2), and the systems expected to undergo Case BC RLOF are found for lower q_i and P_i (Fig. A.1). The major difference compared to the Case B models is the mass of the companion, which here can accrete a few solar masses (compared to $\lesssim 0.5 M_\odot$ for Case B systems) thanks to the tides that spin down the accretor during RLOF. We also observe more significant differences in $M_{\text{He-dep}}$ for models of the same initial mass but different q_i and P_i (cf. Fig. A.1). While the Case B models tend to have neatly separated regions of the mass-radius diagram as a function of the initial mass (cf. Fig. 2), Case A models are more scattered.

In conclusion, we expect to find that Case A systems can undergo Case BC RLOF and reach CC for $14.1 \leq M_{1,i} < 28.2 M_\odot$. Compared to Case B systems (Sect. 3.2), Case A systems are favored by the initial period distribution (Sana et al. 2012), but the need of higher initial masses will make the contribution to the population of systems undergoing Case BC RLOF less important compared to that of Case B systems.

Appendix B: The effect of the secondary star's mass and accretion efficiency during Case BC-RLOF

As initially presented in Sect. 3.2, there is a wide parameter space of interacting binaries which can give rise to a tight-enough HeS + MS binary where the HeS can undergo Case BC RLOF. Our models focused an initial mass ratio $q_i = 0.5$, which is only a subset of the models, and companion masses for HeS donors can have a variety of masses, ranging from a $\lesssim 2 M_\odot$ to $\gtrsim 20 M_\odot$.

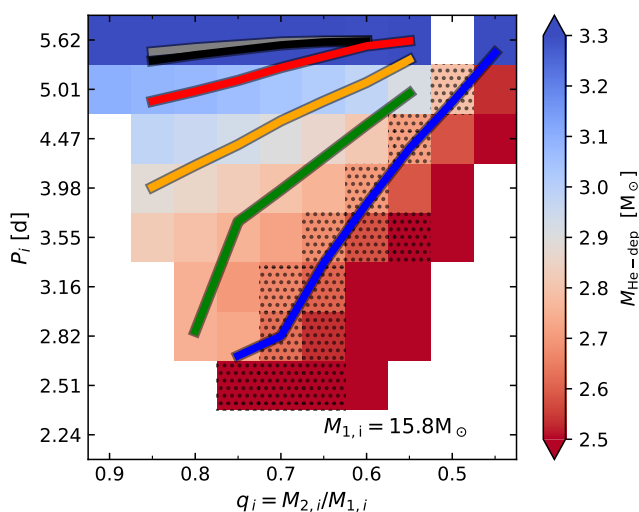


Fig. A.1. The same diagrams shown in Fig. 3 but for Case A systems with $M_{1,i} = 15.8 M_\odot$.

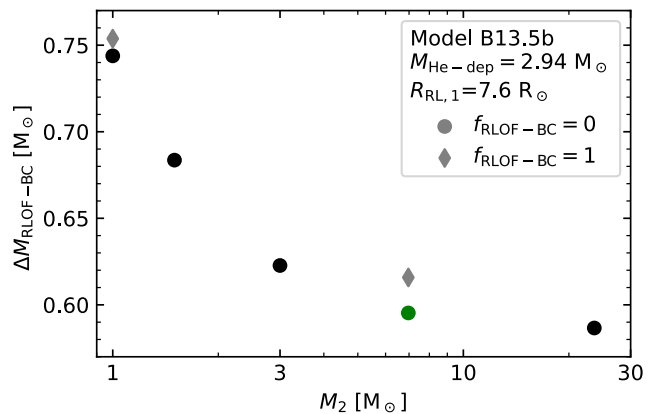


Fig. B.1. Amount of mass shed during Case BC RLOF for model B13.5b (green circle) re-calculated with different companion masses (black circles) and/or accretion efficiency of unity (gray diamonds).

To measure the systematic uncertainty in our estimates on $\Delta M_{\text{RLOF-BC}}$, we rerun model B13.5b (with $M_{\text{He-dep}} = 2.94 M_\odot$ and $M_2 = 6.9 M_\odot$) with a secondary of a different mass M_2 (namely 1, 1.5, 3 and $27 M_\odot$) positioned at an orbital separation such that $R_{\text{RL},1} = 7.6 R_\odot$, the results of which are shown in Fig. B.1. If we maintain mass transfer as inefficient, models with $M_2 \geq 3 M_\odot$ see a negligible difference in $\Delta M_{\text{RLOF-BC}}$ compared to the original run which can be understood in the context of the orbital evolution, as RLOF is occurring from the less massive component to the more massive, causing the orbit to widen. For models where the companion is less massive, $\Delta M_{\text{RLOF-BC}}$ increases by as much as $0.15 M_\odot$. These models, which would correspond to systems which initially had a mass ratio of about 0.11 and 0.08, would have been produced by systems that underwent unstable Case B RLOF, which would have most likely merged. As such, they are representative for the case in which the companion is a compact object, like a NS or BH.

Our choice of $q_i = 0.5$ means that in the vast majority of cases the accretor will be more massive than what we simulated, as lower q_i tend to undergo unstable RLOF before producing a HeS (cf. Sect. 7.2.2). We can therefore expect that in the stable mass transferring channel, $\Delta M_{\text{RLOF-BC}}$ will be similar to the values we estimated. We expect models with significantly less massive companions, like a NS, to have a higher $\Delta M_{\text{RLOF-BC}}$, in the order of $\sim 0.15 M_\odot$ from our expectation.

With regards to the mass-transfer rate before core collapse, we similarly observe small variations compared to the original run when changing the secondary's mass (cf. Fig. B.2). The peak of the mass transfer rate happens earlier on for more extreme mass ratios (shifting by at most 500 yr) reaching values at most $\lesssim 10\%$ higher. The shift of the peak at earlier times result in a more significant drop in the mass transfer rate in the last 100 yr before core-collapse, by as much as a factor 2, which would decrease the probability of interaction-power dominating in the light-curve of the exploding SN with a constantly-expanding CSM (cf. Sect. 5.4). The opposite is instead true for higher-mass companions.

We will focus on the effect of a higher mass transfer efficiency Case BC RLOF. We rerun model B13.5b two times, with a companion M_2 of $1 M_\odot$ and $6.9 M_\odot$ (i.e., that of the original model) and a mass transfer efficiency of 1. As the accretion of pure He on a MS star has proven difficult, we resorted to model this phase by setting the secondary star to a point mass. The

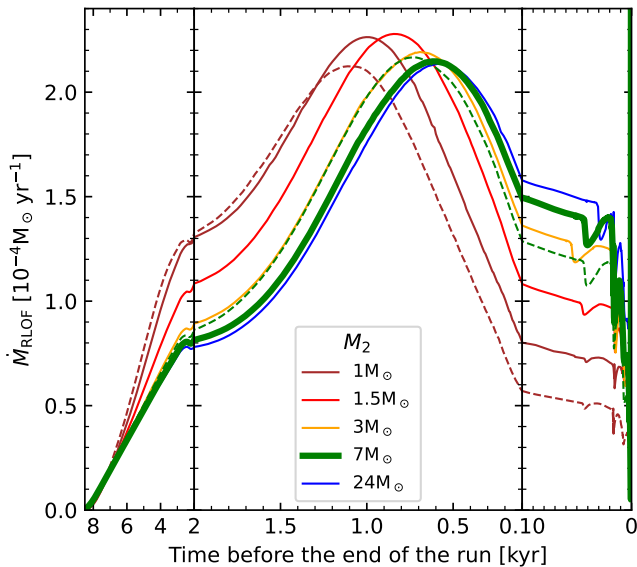


Fig. B.2. Mass transfer rate before the end of the run for model B13.5b (green, thick line) with different secondary masses (see legend). For solid lines indicate the models where mass transfer is assumed inefficient, while the dashed ones assume an accretion efficiency of unity.

amount of mass transferred increased by a negligible amount (cf. Fig. B.2), but this comes at the cost of no CSM being formed around the system at CC, therefore hindering the possibility of interaction features appearing in the SN. If accretion were to be efficient, the secondary star would inevitably show significant He- and N- enrichment on the surface (e.g. Richards et al. 2024) which will be more prominent for less massive companions.

Appendix C: A better parameter to calibrate the outcome of Case BC-RLOF

There is qualitative agreement between the trends in $\Delta M_{\text{RLOF-BC}}$ and the expected time at which the star would fill its Roche lobe, based on the radius evolution of a single HeS model of the same mass (cf. the top panel in Fig. 8). This correlation would be a significant tool to predict $\Delta M_{\text{RLOF-BC}}$ based on a binary-stripped HeS model's $M_{\text{He-dep}}$ and $R_{\text{RL},1}$ and a grid of single HeS models, but it is clear that in the state shown in Fig. 8 it is not significant enough to make useful predictions.

Previous works hinted that single HeS and binary-stripped HeS have qualitative differences in their internal structure, which can affect its radius evolution (e.g., Laplace et al. 2020). We set out to investigate the differences in the internal structure of single HeS and binary-stripped HeS models. The different evolutionary history between the single and binary sets of models can play a role.

We compare models B12.3j, He2.86, and He2.99, which have similar $M_{\text{He-dep}}$ (in B12.3j, $M_{\text{He-dep}} = 2.90 M_{\odot}$) whose main features are shown in Fig. C.1. The range of $M_{\text{He-dep}}$ close to $2.90 M_{\odot}$ exhibits the sharpest difference in radii, especially at later times in the evolution (cf., Fig. 8), and as such even small differences in $M_{\text{He-dep}}$ should result in appreciable differences in the radius evolution. Instead, model B12.3j has an almost-identical radius evolution to that of model He2.86 (cf. Fig. C.1).

Models B12.3j and He2.86 also share a very similar final CO-core mass ($M_{\text{CO,end}} = 1.62 M_{\odot}$) suggesting that the radius evolution may be more closely linked to $M_{\text{CO,end}}$ rather than

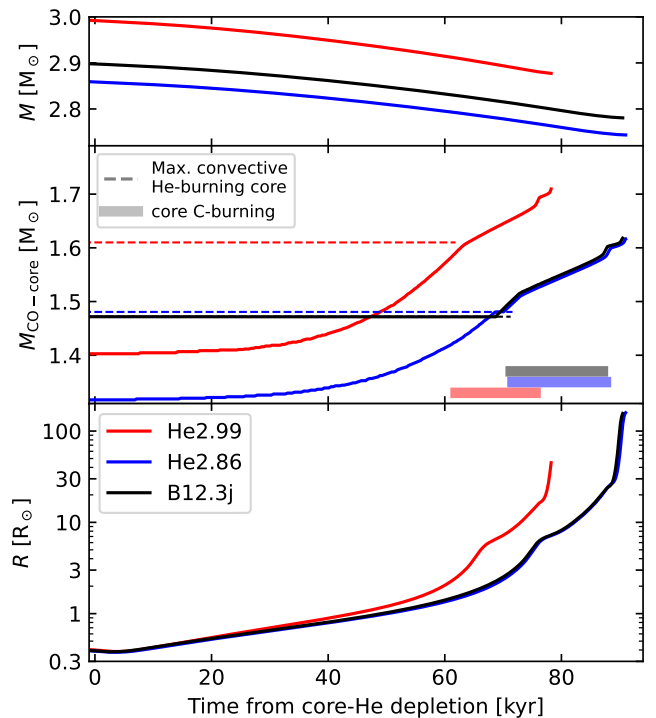


Fig. C.1. Total mass of the HeS (top), CO-core (middle) and radius (bottom) as a function of time, for two single HeS models (He2.97 and He2.83, in red and blue respectively) and one binary-stripped HeS model (B12.3j in black). In the middle panel, $M_{\text{conv,He}}^{\text{max}}$ is shown with dashed lines for each model, and the phase of convective core C-burning is highlighted with horizontal boxes. The models are plotted until the end of the first C-burning shell.

$M_{\text{He-dep}}$. We also observe that M_{CO} is qualitatively different between the single HeS and binary-stripped HeS models (Fig. C.1). The cause of this different evolution stems from the different evolution of the mass of the HeS during core He-burning, caused by the presence of the H-rich envelope in the binary-stripped HeS model.

In the single HeS models, the total mass shrinks monotonically with time, as the winds erode the naked He-rich layers, and so does the extent in mass of the convective core, creating an abundance gradient of He. For the binary-stripped HeS, which retain a thin H-rich envelope, the He-core initially grows in mass (from $2.72 M_{\odot}$ at core H-depletion up to $3.35 M_{\odot}$, see also Fig. 4) before the H-rich envelope is eroded by the winds. This allowed the convective He-burning region to remain constant in mass for a long time, and even expand, before the wind erosion caused it to shrink as well.

This results in a sharper He abundance gradient above the newly formed CO-core for binary-stripped HeS models than single HeS ones. Comparing the maximum extent of the convective He-burning region ($M_{\text{conv,He}}^{\text{max}}$) and the initial mass of the CO-core (cf. Fig. 4, defined as the region where $X_{\text{He}} \leq 0.01$), outlines the shell that showcases a gradient in He and C+O abundances. This region in the single HeS models is about $\sim 0.2 M_{\odot}$ thick, while in B12.3j it is completely missing, indicating therefore the presence of a sharper abundance gradient.

The presence of this gradient allows the single HeS models to steadily increase the CO-core mass over time, while it does not increase for model B12.3j until core C-ignition, at which point the core mass and further evolution match those of model

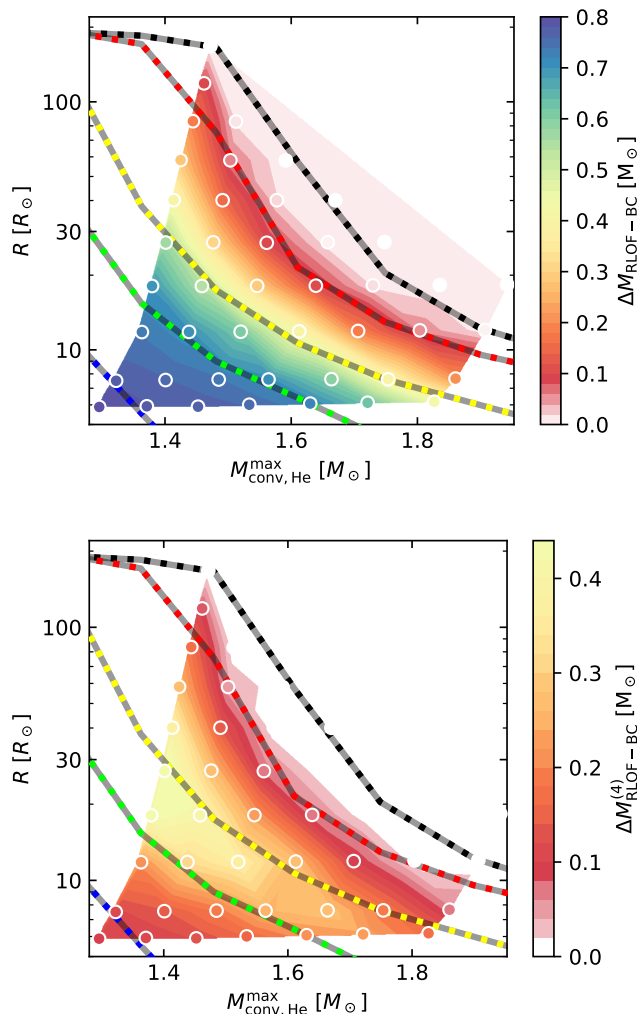


Fig. C.2. The same maps shown in Fig. 8, where the x -axis is $M_{\text{conv,He}}^{\text{max}}$.

He2.86. It seems therefore that $M_{\text{CO-core}}$, and therefore its proxy-quantity $M_{\text{conv,He}}^{\text{max}}$ are better parameters to predict the radius evolution of a HeS. The latter quantity is already available during core He-burning, and therefore less expensive to compute compared to $M_{\text{CO-core}}$.

If we adopt $M_{\text{conv,He}}^{\text{max}}$ rather than $M_{\text{He-dep}}$ as the quantity to calibrate for the expected maximum radii, we can redraw Fig. 8 in Fig. C.2, which now shows a much better general agreement between the trends for $\Delta M_{\text{RLOF-BC}}$ and the radius evolution of single HeS models.

These results, plus the solidity of our estimates when changing the companion mass (cf. Appendix B), show the general predictive power of our comparison. We warrant however that for lower masses outside the simulated region, Fig. C.2 shows that the trends would suggest a stronger degree of mass-loss than expected.

Appendix D: He/CO shell merger and Case X RLOF

One peculiar behavior that arises in some of our models (and also found in others in the literature, such as Tauris et al. 2013, 2015; Wei et al. 2024; Guo et al. 2024 and, more interestingly, WF22) is the presence of a final mass transfer event, which we labeled as Case X RLOF, shortly before CC. As noted in Sect. 4.1.3 and

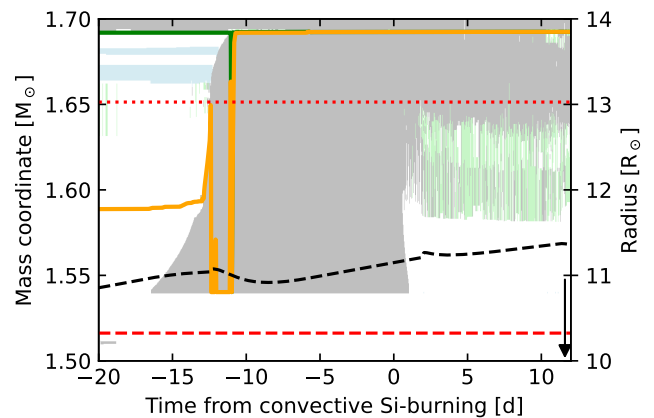


Fig. D.1. The same Kippenhahn plot shown in Fig. 5 for system B13.5b (Sect. 4.1) and rerun from core O-depletion without any overshooting. The zero point in the x -axis is set to the onset of convective core Si-burning. The black arrow shows the moment when core Si-burning ends.

4.2.3, this phase of mass transfer is commonly linked to the He-burning shell digging significantly inside the CO-core, which is also observed in more massive models in the literature (e.g., Wu & Fuller 2021).

We argue that this phenomenon is likely caused by the use of overshooting in the model. To test this, we ran the model discussed in Sect. 4.1 from the time of core O-depletion, and deactivated overshooting. The following evolution in terms of the development of the subsequent shells is similar, with some slight differences. We will focus exclusively on the effects close to the CO/He interface.

As noted already in Sect. 4.1.3, Ne begins burning at a mass coordinate of $1.54 M_{\odot}$ roughly a month prior to the end of the run, and it develops a convective region on top of it. This region extends above the Ne/O rich meshes (extending up to $1.59 M_{\odot}$) mixing also the meshes that still retain residual C until the He/CO interface. Here, differently from the original model, He is not ingested inside this convective region, and the envelope's composition and extension remain unaltered (cf., Fig. D.1). At the onset of convective Si-burning this convective region dies off.

This model showcases two main differences with the original one showed in Sect. 4.1. Not only did the shell merger not occur, but the lifetime of the model also changed dramatically. The original model, following the onset of this external Ne-burning region, would have to wait for another ~ 200 d to ignite Si convectively, as the core's internal structure is affected following the sudden mass-loss and core-erosion. Without these sudden changes to the stellar structure, convective Si burning begins only two weeks after the onset of the external Ne-burning shell, and the model even reaches core-Si depletion, just 11 days after.

In this section we show that the implementation of over- and undershooting is the direct cause for the anomalous behavior experienced in the model. We caution that it remains to be seen if these results also hold in the case of models with a different nuclear network, as the shell structure would change. It is however important to mention that the general phenomenon of shell mergers appears in 3D-hydro simulations (e.g., between the C and Ne/O shells in Yadav et al. 2020), and therefore warrants further study.

Regardless of the cause of Case X RLOF, it has already been present in previous models in the literature, though with different

features and timescales, such as WF22 and Guo et al. (2024) for HeS+NS systems. In their models, no shell merger is mentioned to occur, and yet a final phase of mass transfer ensues nonetheless about $\sim 10 - 50$ yr prior to core Si-ignition and the onset of an EC-SNe respectively. Other models have exhibited such He/C shell-merger, like Habets (1986) and Woosley et al. (1995), without necessarily exhibiting this expansion phase. This may then indicate that the shell-merger we observed in the models is perhaps one of many symptoms that can cause this expansion and thus Case X RLOF.

Appendix E: Additional effects on the SN

Appendix E.1: Spin-down of the newborn NS

One process that may affect the explosion is the rapid spin-down of the newly-born NS (e.g. Metzger et al. 2015). We assume angular momentum conservation during CC, such that the newly-born NS will retain the same specific angular momentum of the inner $1.35 M_{\odot}$ of the core.

The models that have undergone little to no mass transfer retain an average specific angular momentum of the order of $10^{13} - 10^{14} \text{ cm}^2 \text{ s}^{-1}$. Assuming the newborn NS has a radius of ~ 15 km, a mass of $1.35 M_{\odot}$ and therefore a moment of inertia of $\sim 2 \times 10^{45} \text{ g cm}^2$ (adopting Eq. 19 from Worley et al. 2008), this results in a final spin period of $\sim 0.01 - 1$ s. The moment of inertia is compatible with the amount estimated for the youngest observed galactic NSs (Heger et al. 2005), while the spin-period is one or more orders of magnitude lower than the 1 ms period expected to provide significant power to the supernova explosion (Metzger et al. 2015). The models that lost more mass have lower moment of inertia ($10^{10} - 10^{13} \text{ cm}^2 \text{ s}^{-1}$) and therefore produce an even slower spinning NS (with P_{spin} from 1 to 1000 s) which would be too slow to develop significant effects to the SN.

Appendix E.2: The effect of a close MS companion

The presence of a close-by MS star at the time of the explosion may affect the SN, as the ejecta rams with the companion star. While this has been predicted in the context of Type Ia SNe (see Liu et al. 2023, for a review), one of the first observations hinting at this process for CCSNe was recently reported for the Type Ic SN2022jli (Moore et al. 2023; Chen et al. 2024). The peculiarity of this object lies in the 12.4 d modulation of the light-curve. The extended observations presented in Chen et al. (2024) showcase an abrupt decline in the light-curve luminosity (after ~ 300 d), which they argue is compatible with a shortly-lived phase of mass transfer between the MS companion, thrown off of equilibrium by the impacting ejecta, and the newly-formed compact object gulping material during the passage at periastron.

Since all of our SN progenitors are in orbit with a MS companion, this effect may be present for the tighter systems at CC. In our models, the companion typically subtends up to 1% of the field of view. Assuming an explosion energy of $\sim 6 \times 10^{50}$ erg, the secondaries may capture as much as $\sim 6 \times 10^{48}$ erg of energy, of which only $\sim 10\%$ may be injected inside the stellar structure to drive its expansion (cf., Hirai et al. 2018; Hirai 2023, the remaining is instead injected onto the unbound material, which may be as much as $\lesssim 0.01 M_{\odot}$). If we apply these estimates to the empirical model fits in Ogata et al. (2021), the companion may swell to as much as $\sim 1000 R_{\odot}$, with a very short-lived expansion of at most a few years, which is of the same order of magnitude as the timescale for the luminosity drop in SN 2022jli (Chen et al. 2024).

As the impact with the MS companion will unbind some of its H-rich envelope (Liu et al. 2015; Hirai et al. 2018), we expect that the SNe from our models should showcase narrow H-line emission at late times in the evolution of the SN.

Appendix F: Interaction-powered luminosity

Let's assume that the mass un-accreted during Case BC RLOF is ejected from the system, and that it moves at a constant velocity v_{CSM} . At $t = 0$, the SN explosion will expel a fast moving shell (i.e., the ejecta) with initial mass M_{ej} and initial (bulk) velocity v_{ej} , which will gradually sweep the CSM as it travels through it. We will follow the evolution of the portion of the fast-moving shell that interacts with the CSM. We will refer to it as the cold dense shell (CDS, Chugai et al. 2004), which has an initial mass $M(0) = M_{\text{ej}} \sin \theta$ (depending on the opening angle of the CSM, cf. Sect. 5.3), and velocity $v(0) = v_{\text{ej}}$. We assume that the CDS collides inelastically with the CSM, thus conserving momentum while losing kinetic energy which we assume is completely converted into radiation. We neglect any effect from photon-diffusion processes, and we only focus on the rate of energy loss from the CDS. Under this assumption, the amount of kinetic energy that is converted into radiation as the CDS sweeps through a small shell of mass dm is equal to

$$dE = \frac{1}{2} M v^2 + \frac{1}{2} dm \cdot v_{\text{CSM}}^2 - \frac{1}{2} (M + dm) \left(\frac{Mv + dm \cdot v_{\text{CSM}}}{M + dm} \right)^2. \quad (\text{F.1})$$

Performing a series expansion for dm , under the assumption that at any given time interval dt we have $dm \ll M$, results in

$$dE = \frac{1}{2} dm (v - v_{\text{CSM}})^2, \quad (\text{F.2})$$

which, if divided by the time interval, gives the interaction luminosity

$$L_{\text{inter}} = \frac{dE}{dt} = \frac{1}{2} \frac{dm}{dt} (v - v_{\text{CSM}})^2 \quad (\text{F.3})$$

We can write a differential equation for the CDS's velocity v per conservation of momentum, as

$$\frac{dv}{dt} = - \frac{dm}{dt} \frac{v(t) - v_{\text{CSM}}}{M(t)}. \quad (\text{F.4})$$

The CDS's mass M will also increase over time, as the CDS gradually sweeps material from the CSM

$$\frac{dM}{dt} = \frac{dm}{dt}. \quad (\text{F.5})$$

Once $\frac{dm}{dt}$ is known, Eq. F.4 and F.5 form a complete set of differential equations, once we include the initial conditions $M(0)$ and $v(0)$. Solving for $M(t)$ and $v(t)$, then $L_{\text{inter}}(t)$ can be evaluated using Eq. F.3. Note that the information on the geometry of the CSM is found inside dm and the initial condition on the CDS's mass.

We will now describe the mass-element of the CSM, assuming this was either constantly expanding following mass loss from the inner binary or a CBD, and derive L_{inter} for each case.

Appendix F.1: Free-moving CSM

If we assume that the CSM is polluted following mass-loss, with the material moving away from the system, we can use the mass-loss history of the system to infer the swept up mass dm per unit time dt .

To know the time at which the material dm was ejected before CC (t_{RLOF}), one needs to solve the following integral equation, where the moment of CC is set to 0,

$$\int_{-t_{\text{RLOF}}}^t v_{\text{CSM}}(t') dt' = \int_0^t v(t') dt'. \quad (\text{F.6})$$

As we have no constrain on v_{CSM} , we assume it is for simplicity constant. With this, we can take the derivative of the previous equation by t to obtain the following differential equation

$$\frac{dt_{\text{RLOF}}}{dt} = \frac{v(t) - v_{\text{CSM}}}{v_{\text{CSM}}}, \quad (\text{F.7})$$

where a physical solution exists as long as $v(t) > v_{\text{CSM}}$. This provides a scaling factor between the mass-loss rate from the system $\dot{M}_{\text{RLOF}} = \frac{dm}{dt_{\text{RLOF}}}$ and the amount of mass swept by the CDS as it travels through the CSM per unit time

$$\frac{dm}{dt} = \frac{dm}{dt_{\text{RLOF}}} \frac{v(t) - v_{\text{CSM}}}{v_{\text{CSM}}} = \dot{M}_{\text{RLOF}}(t_{\text{RLOF}}) \frac{v(t) - v_{\text{CSM}}}{v_{\text{CSM}}}, \quad (\text{F.8})$$

where we retrieve \dot{M}_{RLOF} from the model by looking up the mass-loss rate at a time t_{RLOF} prior to CC by solving Eq. (F.7). Substituting this back in Eq. (F.3) yields

$$L_{\text{inter}}(t) = \frac{1}{2} \dot{M}_{\text{RLOF}}(t_{\text{RLOF}}(t)) \frac{(v(t) - v_{\text{CSM}})^3}{v_{\text{CSM}}}. \quad (\text{F.9})$$

For the generic solution, Eq. (F.9) needs to be coupled with Eq. (F.7), and the differential equations for the velocity and mass of the CDS (Eq. (F.4) and (F.5)) which are given by

$$\begin{cases} \frac{dv}{dt} = -\frac{(v(t) - v_{\text{CSM}})^2}{v_{\text{CSM}}} \frac{\dot{M}_{\text{RLOF}}(t_{\text{RLOF}}(t))}{M(t)}, \\ \frac{dM}{dt} = \dot{M}_{\text{RLOF}}(t_{\text{RLOF}}(t)) \frac{v(t) - v_{\text{CSM}}}{v_{\text{CSM}}} \end{cases}, \quad (\text{F.10})$$

and we have to add the initial condition for the differential equation Eq. (F.7), that is $t_{\text{RLOF}}(0) = 0$.

Appendix F.2: CSM bounded in a CBD

We can assume that M_{CSM} is bounded within a CBD (or, more precisely, a torus) of internal radius R_{in} , outer radius R_{out} and opening angle θ . We assume that the material inside the CBD has no bulk movement, such that $v_{\text{CSM}} = 0$. We write the mass-element as follows:

$$dm = 4\pi \sin \theta \rho(r) r^2 dr. \quad (\text{F.11})$$

Let us work under the assumption that $\rho(r) = \rho_0 \left(\frac{r}{R_{\text{in}}}\right)^s$, with ρ_0 as the characteristic density at a distance R_{in} , which is equal to

$$\rho_0 = \begin{cases} M_{\text{CSM}} \left[\frac{4\pi}{3+s} R_{\text{in}}^{-s} (R_{\text{out}}^{3+s} - R_{\text{in}}^{3+s}) \sin \theta \right]^{-1} & s \neq -3 \\ M_{\text{CSM}} \left[4\pi R_{\text{in}}^3 \left(\ln \frac{R_{\text{out}}}{R_{\text{in}}} \right) \sin \theta \right]^{-1} & s = -3 \end{cases}. \quad (\text{F.12})$$

We define the following quantity

$$\mathcal{R}^{(p)} = \begin{cases} \frac{1}{p} (R_{\text{out}}^p - R_{\text{in}}^p) & p \neq 0 \\ \ln(R_{\text{out}}/R_{\text{in}}) & p = 0 \end{cases} \quad (\text{F.13})$$

which carries the information of a length to the power of p . We thus obtain the following form for the mass-element

$$dm = M_{\text{CSM}} \frac{r^{2+s} dr}{\mathcal{R}^{(3+s)}} \quad (\text{F.14})$$

We now have all the information necessary to rebuild the differential equations Eqs. F.4-F.5, by writing $v(t) = \frac{dr}{dt}$, which are

$$\begin{cases} \frac{dM}{dt} = M_{\text{CSM}} v(t) \frac{r(t)^{2+s}}{\mathcal{R}^{(3+s)}} \\ \frac{dv}{dt} = -\frac{M_{\text{CSM}}}{M(t)} v^2(t) \frac{r(t)^{2+s}}{\mathcal{R}^{(3+s)}} \end{cases} \quad (\text{F.15})$$

And finally, combining Eqs. F.3 and F.15 yields

$$L_{\text{inter}}(t) = \frac{1}{2} M_{\text{CSM}} v^3(t) \frac{r(t)^{2+s}}{\mathcal{R}^{(3+s)}}. \quad (\text{F.16})$$

Do note that, because of the assumption that the disk is stationary, the equation for conservation of momentum simplifies to

$$M(t)v(t) = M(0)v(0) = M_{\text{ej}} \sin \theta v_{\text{ej}} \quad (\text{F.17})$$

making one of the equations in Eq. (F.15) redundant. We use Eq. (F.17) to get rid of $M(t)$ in the equations. We therefore only need to solve the equation of motion of the CDS, which is a second-order non-linear differential equation

$$\ddot{r} = -\frac{M_{\text{CSM}}}{M_{\text{ej}} \sin \theta} \frac{1}{v_{\text{ej}}} \frac{1}{\mathcal{R}^{(3+s)}} \dot{r}^3 r^{2+s} \quad (\text{F.18})$$

where $\ddot{r} = dv/dt$ and $\dot{r} = v(t)$. It is possible to obtain the generic (albeit implicit) solution

$$c_1 r(t) + \frac{1}{4+s} \frac{1}{3+s} \frac{M_{\text{CSM}}}{M_{\text{ej}} \sin \theta} \frac{1}{v_{\text{ej}}} \frac{r(t)^{4+s}}{\mathcal{R}^{(3+s)}} = t + c_2 \quad (\text{F.19})$$

where c_1 and c_2 can be determined using the initial conditions at $t_0 = \frac{R_{\text{in}}}{v_{\text{ej}}}$ which are $r(t_0) = R_{\text{in}}$ and $v(t_0) = v_{\text{ej}}$. We can therefore write the analytical expressions for $r(t)$ and $v(t)$ as

$$\begin{cases} r(t) - v_{\text{ej}} t = \frac{M_{\text{CSM}}}{M_{\text{ej}} \sin \theta} \left[\frac{R_{\text{in}}^{s+3} (r(t) - R_{\text{in}})}{R_{\text{out}}^{3+s} - R_{\text{in}}^{3+s}} - \frac{1}{4+s} \frac{r(t)^{4+s} - R_{\text{in}}^{4+s}}{R_{\text{out}}^{3+s} - R_{\text{in}}^{3+s}} \right] \\ v(t) = v_{\text{ej}} \left(1 + \frac{M_{\text{CSM}}}{M_{\text{ej}} \sin \theta} \frac{r(t)^{3+s} - R_{\text{in}}^{3+s}}{R_{\text{out}}^{3+s} - R_{\text{in}}^{3+s}} \right)^{-1} \end{cases} \quad (\text{F.20})$$

Appendix G: Other SNe

In the main text (Sect. 6) we only focused on Type Ibn and Icn SNe. Here, we will also report other SNe that show interaction features, namely the low-energy USSNe and Ca-rich transients (CaRTs, Appendix G.1) and SLSNe (Appendix G.2).

Appendix G.1: USSNe and CaRTs

The group of low-energy SNe includes the subclasses of USSNe and CaRTs, of which some are discussed in the literature as showing interaction features. Both groups are usually understood as low-mass He-stars undergoing CC or WD-related events (e.g., double WD mergers or single-WD detonation/deflagration scenarios, De et al. 2020; Jacobson-Galán et al. 2022) based on the

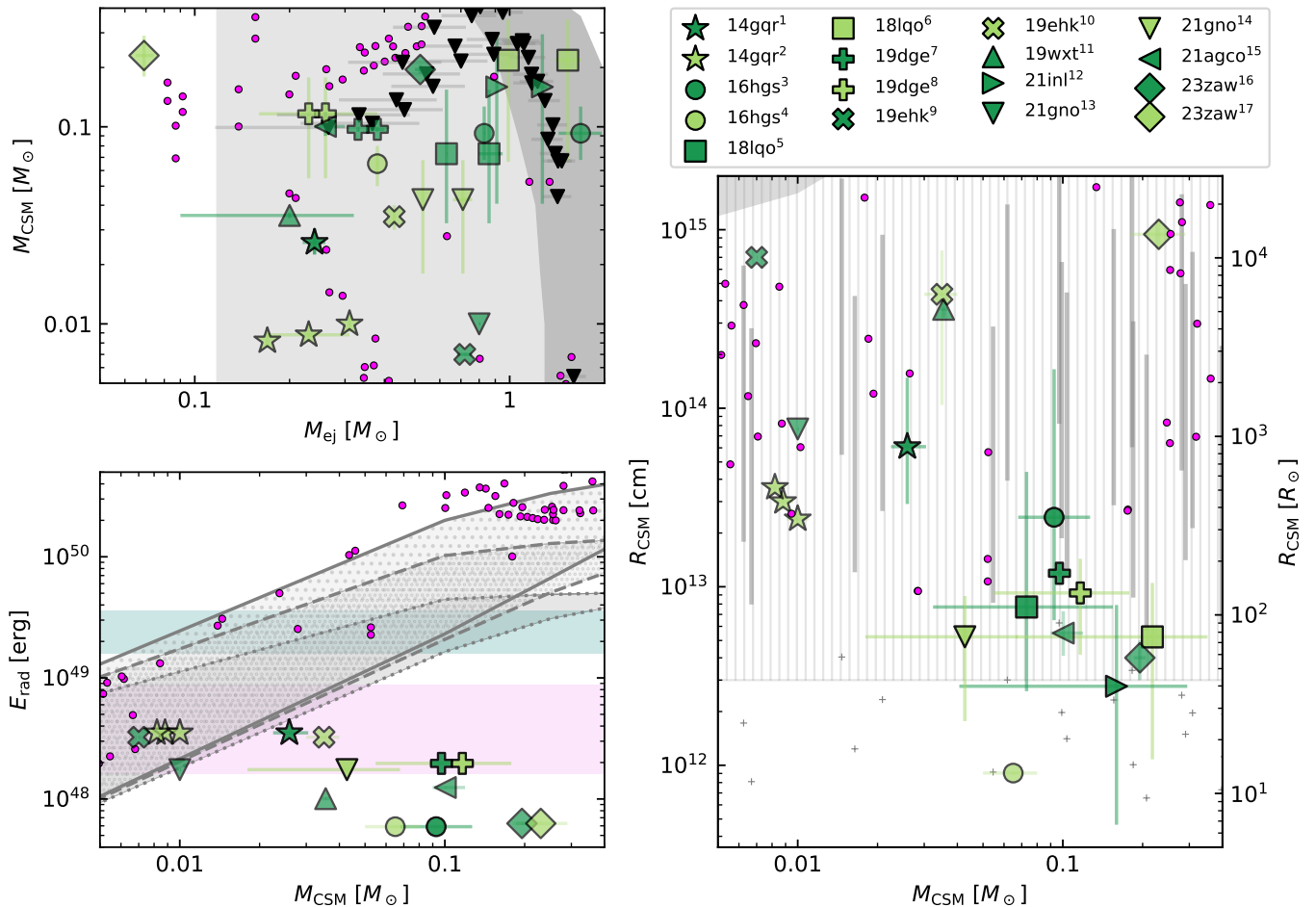


Fig. G.1. The same as Fig. 14 but for USSNe and CaRTs.

References:; iPTF14gqr: (1) Yao et al. 2020; De et al. 2018b (2) De et al. 2018b; iPTF16hgs: (3) Yao et al. 2020; De et al. 2018a (4) De et al. 2018a; SN2018lqo: (5) Yao et al. 2020 (6) Das et al. 2024b; SN2019dge: (7) Yao et al. 2020 (8) Das et al. 2024b; Yao et al. 2020; SN2019ehk: (9) Jacobson-Galán et al. 2020 (10) Nakaoka et al. 2021; Jacobson-Galán et al. 2020; SN2019wxt: (11) Shivkumar et al. 2023; SN2021inl: (12) Das et al. 2024b; SN2021gno: (13) Ertini et al. 2023 (14) Das et al. 2024b; SN2021agco: (15) Yan et al. 2023; SN2023zaw: (16) Das et al. 2024a (17) Moore et al. 2024

lack of local star-formation. The CaRTs are additionally distinguished by the presence of strong Ca-lines in the spectra. Many of these objects are classified as both USSNe and CaRTs (e.g., SN2019ehk, Nakaoka et al. 2021), and we therefore discuss these two groups together. Of the observed USSNe and CaRTs, we report those that show interaction features, like a double-peak morphology in their light curves (Das et al. 2024b).

For each event, the multiple estimates of M_{ej} stem from works where they fit with different light-curve models (Arnett 1982 or Khatami & Kasen 2019), and produce results differing by at most $\sim 50\%$ (cf. Fig. G.1) with the bulk found between 0.2 and $1.5 M_{\odot}$. The value of M_{CSM} is inferred to below $0.3 M_{\odot}$ for all the events. Considering that our estimates for M_{CSM} are understood as upper-limits, our models are compatible with the inferred values of M_{ej} and M_{CSM} for each event, with one exception being SN 2023zaw, which has a very small inferred M_{ej} .

The inferred extension of the CSM of these SNe is quite varied, but overall consistent with a CBD-like CSM from our models. The most extended CSM inferred from observations reach 10^{15} cm, while many objects instead have much lower inferred extensions of ($3 \times 10^{12} - 10^{14}$ cm). More than half share similar $M_{\text{CSM}} \sim 0.1 M_{\odot}$ and $R_{\text{CSM}} \sim 10^{13}$ cm, within a factor two. The

only observation falling outside our scenario is iPTF16hgs, for which De et al. (2018a) infer the CSM being found within $10 R_{\odot}$, which can instead be explained in the context of shock-cooling of an extended envelope. However, the other estimates from Yao et al. (2020) for the same event put it within our expected parameter space.

The light curves of these objects are dim, resulting in radiated energies of $\sim 10^{48}$ erg (cf. Fig. G.1), close to or just lower than what than expected for typical Type Ibc SNe (Nicholl et al. 2015). The explosion energy of some of these objects is also low, to about $\lesssim 2 \times 10^{50}$ erg like iPTF16hgs (De et al. 2018a), iPTF14gqr (De et al. 2018b) and SN 2019dge (Yao et al. 2020). Some are inferred as even less energetic, down to $\sim 10^{49}$ erg for SN 2023zaw (Moore et al. 2024). These values are smaller than our fiducial value, but not necessary in tension as we are over-estimating the explosion energies of the most stripped models (Sect. 4.3). Lower conversion efficiencies and small opening angles for a CBD-like CSM can help explain the bulk of the SNe with higher M_{CSM} ($\sim 0.1 M_{\odot}$, cf. Fig. G.1).

We can conclude that almost all of the observed USSNe and CaRTs have inferred properties that can be explained in the context of Case BC RLOF, only with a CBD-like CSM.

Appendix G.2: SLSNe-I

We briefly discuss here the most energetic H-poor events, namely SLSNe, characterized by total radiated energies in the order of 10^{51} erg, which exceed by 10-100 times the values expected in typical Type Ibc SNe (e.g., [Nicholl et al. 2015](#)). These energies are in the order of the kinetic energy of the ejecta in normal SNe, and as such one of the pictures to explain these observed SLSNe is that of the ejecta ramming into a very massive CSM (see Sect. 5.3).

The SLSNe-I typically have inferred CSM masses that are much larger than expected from any HeS progenitor formed through our binary channel ($M_{\text{CSM}} = 4.67 \pm_{2.56}^{6.90} M_{\odot}$ [Chen et al. 2023](#)), which points to a different kind of progenitors than the ones we introduce in this work. Furthermore, in many of these SNe the contribution of the spin-down of a newly born magnetar can fit the light-curves well ([Gomez et al. 2024](#)) if not even better than the CSM-scenario ([Chen et al. 2023](#)), while the process is not expected to contribute in our models (cf Appendix. E.1). With this, we conclude that SLSNe-I are hard to reconcile with CSM interaction in the context of the models explored in this work.